Thermomechanical Finite-Element Model of Shell Behavior in Continuous Casting of Steel

CHUNSHENG LI and BRIAN G. THOMAS

A coupled finite-element model, CON2D, has been developed to simulate temperature, stress, and shape development during the continuous casting of steel, both in and below the mold. The model simulates a transverse section of the strand in generalized plane strain as it moves down at the casting speed. It includes the effects of heat conduction, solidification, nonuniform superheat dissipation due to turbulent fluid flow, mutual dependence of the heat transfer and shrinkage on the size of the interfacial gap, the taper of the mold wall, and the thermal distortion of the mold. The stress model features an elastic-viscoplastic creep constitutive equation that accounts for the different responses of the liquid, semisolid, delta-ferrite, and austenite phases. Functions depending on temperature and composition are employed for properties such as thermal linear expansion. A contact algorithm is used to prevent penetration of the shell into the mold wall due to the internal liquid pressure. An efficient two-step algorithm is used to integrate these highly nonlinear equations. The model is validated with an analytical solution for both temperature and stress in a solidifying slab. It is applied to simulate continuous casting of a 120 mm billet and compares favorably with plant measurements of mold wall temperature, total heat removal, and shell thickness, including thinning of the corner. The model is ready to investigate issues in continuous casting such as mold taper optimization, minimum shell thickness to avoid breakouts, and maximum casting speed to avoid hot-tear crack formation due to submold bulging.

I. INTRODUCTION

COMPUTATIONAL models are important tools to gain insight into thermal and mechanical behavior during complex manufacturing processes such as the continuous casting of steel billets. This process features many interacting phenomena which challenge modeling methods, shown in Figure 1(a). Starting with the turbulent flow of molten steel into the mold cavity, superheat is dissipated during flow recirculation in the liquid pool prior to solidifying a shell against the walls of a water-cooled copper mold. Heat transfer is controlled by conduction through the solidifying steel shell, the mold, and, especially, the size and properties of the interfacial layers between them. After initial solidification at the meniscus, the shell tends to shrink away from the mold walls due to thermal contraction. Over most of the strand surface, internal "ferrostatic pressure" from the head of molten metal maintains good contact between the shell and the mold. However, shrinkage near the corners may create gaps or intermittent contact, which greatly lowers the local cooling rate. The extent of the gap depends on the composition-dependent shrinkage of the steel shell, its creep resistance, the casting speed, taper of the mold wall, thermal distortion of the mold wall, and the thermal properties of the material filling the interfacial gap. The mechanical behavior of the shell also controls the formation of defects such as hot-tear cracks and breakouts and depends on thermal shrinkage, high-temperature inelastic stress-generation rate, solid-state phase transformations, temperature, steel composition, multidimensional stress state, and deformation rate. The harsh environment of the steel plant makes it difficult to conduct experiments during the process. To improve insight into these phenomena demands sophisticated mathematical models, to aid the traditional tools of physical models, lab, and plant experiments.

A thermal-mechanical finite-element model that incorporates the aforementioned phenomena, named CON2D, has been developed in the Metals Processing Simulation Laboratory at the University of Illinois at Urbana-Champaign over the past decade[1–4] with several applications.[5–12] After a brief literature review, this article describes the features of the CON2D model. It then presents its validation with analytical solutions and a simulation of a continuous steel billet casting process, where plant measurements were available for comparison.

II. PREVIOUS WORK

Many previous computational models have investigated thermal stress during the continuous casting of steel, including models of billet casting,[13–19] beam blanks,[20] slab casting,[2,6,11,13,14,21–31] and thin-slab casting.[32,33,34] Brimacombe, Grill, and co-workers first applied computational thermal-stress models of a two-dimensional (2-D) billet section under plane stress[13,14] as it moved down the caster. These and similar early models[21,22,23] revealed important insights into crack formation, such as the need to avoid reheating. This infant stage of computational stress modeling was qualitative due to the lack of material properties at high temperature, a simple elastic-plastic constitutive model, and coarse meshes due to computer limitations.

Rammerstorfer *et al*. added a separate creep function in developing a thermoviscoelastic-plastic stress model of a transient one-dimensional (1-D) slice domain through a

CHUNSHENG LI, Postdoctoral Student, and BRIAN G. THOMAS, Wilkins Professor of Mechanical Engineering, are with the Department of Mechanical and Industrial Engineering, University of Illinois at Urbana-Champaign, Urbana, IL 61801. Contact e-mail: bgthomas@uiuc.edu

Manuscript submitted August 18, 2003.

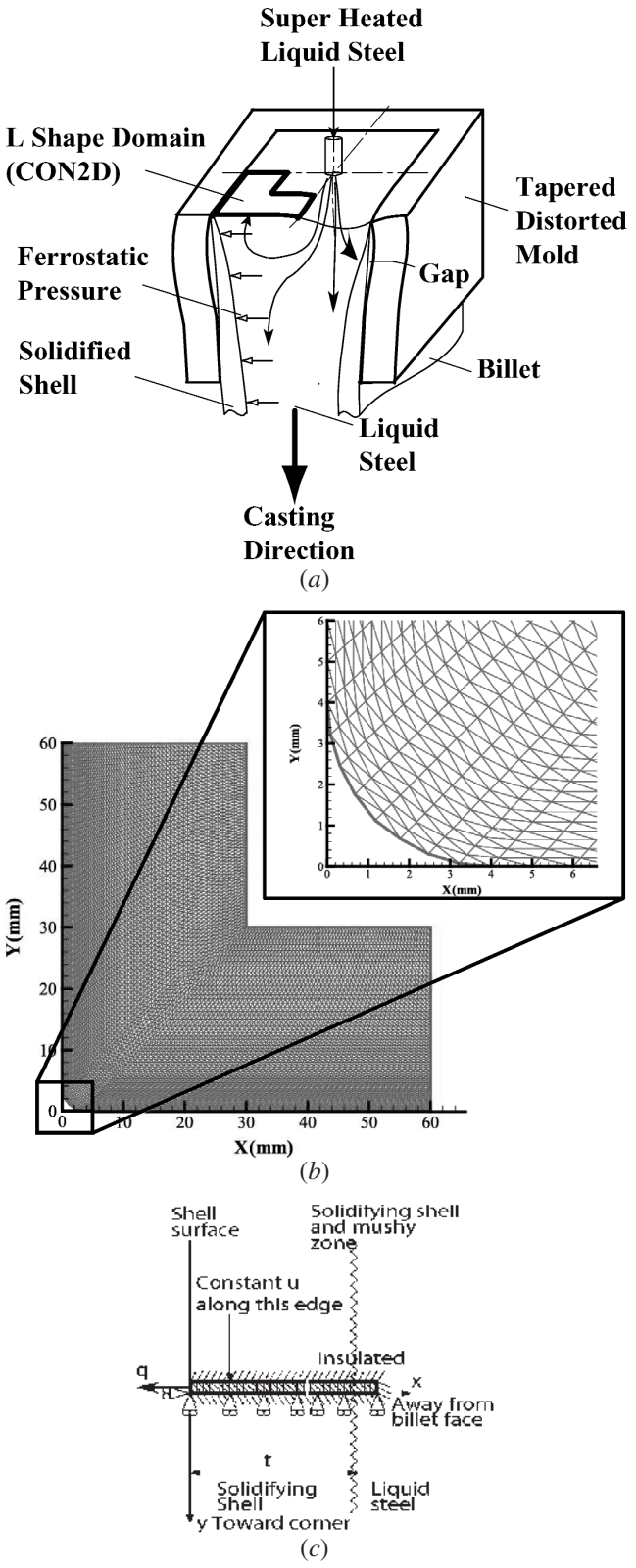

Fig. 1—Modeling domain of casting billet: (*a*) schematic of billet casting, (*b*) L-shaped mess of three-node heat-transfer elements (shown) connected into six-node stress elements, and (*c*) schematic of slice domain at the billet centerline.

slab.[24] Kristiansson[15] advanced the traveling-slice model with stepwise coupling of the thermal and stress computations within a 2-D billet section, based on the interfacial gap between the mold and shell. This model also featured different creep constants for modeling austenite and δ-ferrite and temperature-dependent properties. Similar models were developed for slab sections,[26] including some that assumed plane strain.[27] Kelly *et al*.[16] developed an axisymmetric model of coupled thermal stress in round billets to study the effect of carbon content on the formation of longitudinal cracks. Elastic-stress analysis was performed on the mold and the billet to determine the interfacial-gap profile, followed by elastic-plastic stress analysis of the billet.

Recently, several improved models of the thermal-mechanical behavior of continuous-cast steel have been developed. Boehmer *et al*.[17] coupled a three-dimensional (3-D) in-house heat-flow model and a 2-D thermal-stress model in the ADINA model, to analyze a continuous-cast billet section in plane stress. An elastoplastic constitutive model was adopted, including strain-rate-dependent strength and plasticity, and a separate creep model, if necessary. The solidifying solid was discretized with a deforming grid, and liquid elements were deleted from the stress simulation.

A transverse-slice model, AMEC2D, was developed to simulate beam-blank casting, including elastic-viscoplastic behavior and a simple fluid-flow model to account for superheat transport in the liquid pool.[20] Park *et al*. applied AMEC2D to investigate the effect of mold-corner radius on shell growth and longitudinal corner cracks in billets.[18] This model assumed plane stress and neglected the effects of superheat variations.

Huespe *et al*. developed the Arbitrary Lagrangian-Eulerian[31] and mixed Eulerian-Lagrangian[19] thermal-mechanical models, to analyze stress/strain distributions in continuous-cast round steel billets. These rigorous models adopt elastic-viscoplastic material behavior with temperature- and history-dependent material parameters, but are computationally intensive and assume 2-D axisymmetry. They show that the generalized plane-strain assumption matches closest to the real behavior, short of a full 3-D analysis.

Many important related aspects of continuous casting have been modeled in depth and are discussed elsewhere,[35,36] including fluid flow in the molten steel pool,[37] nonequilibrium solidification of the shell,[35,38] thermal distortion of the mold,[39] bulging and bending of the strand below the mold,[40,41] and crack prediction.[35,42]

Although they have generated important insights, previous thermal-mechanical models of shell solidification in the mold still oversimplify some phenomena or are too computationally expensive to simulate large-scale problems with sufficient mesh and time-step refinement to be accurate. There is still a need for better models to gain more quantitative insight into thermal-mechanical behavior and crack prediction in continuous casting of steel.

III. GOVERNING EQUATIONS

The model solves the transient heat-conduction equation and corresponding force-equilibrium equation for temperature, displacement, strain, and stress in a transverse Lagrangian reference frame moving downward with the steel shell at the casting speed, as shown in Figure 1(a). Both 2-D and 1-D slice domains are simulated, as shown in Figures 1(b) and (c), respectively.

A. *Heat-Transfer and Solidification Model*

The model first solves the transient energy balance (Eq. [1]), where $H(T)$ and $k(T)$ are the isotropic temperature-dependent enthalpy and conductivity, respectively.[43]

$$\rho\frac{\partial H(T)}{\partial T} = \nabla\cdot(k(T)\nabla T) \qquad [1]$$

A 2-D simplification of the full 3-D process is reasonable, because axial (z direction) heat conduction is negligible relative to advection at the high Péclet number of this steel continuous casting process ($vL/\alpha = 2\times 10^3$).*

*v = 0.0167 m/s, L = 1 m, ρ = 7500 kg/m^3, c_p = 0.6 kJ/kgK, K = 40 W/mK.

Applying the chain rule to the left-hand side of Eq. [1] isolates the specific heat (c_p) and latent heat (L_f) together in a convenient function, $\partial H(T)/\partial T$, in Eq. [2]. Heat-balance numerical errors are lessened by providing an enthalpy-temperature look-up function.

$$\rho\left(\frac{\partial H(T)}{\partial T}\right)\left(\frac{\partial T}{\partial t}\right) = \frac{\partial}{\partial x}\left(k(T)\frac{\partial T}{\partial x}\right) + \frac{\partial}{\partial y}\left(k(T)\frac{\partial T}{\partial y}\right) \qquad [2]$$

Boundary conditions can be a fixed temperature, heat flux, convection, or a heat-resistor model across the interfacial layer between the mold wall and the steel surface.[43] The latter enables the fully coupled heat-transfer and stress analysis described in Section VII–C. The thermal-property functions of different steels, including conductivity and enthalpy, are given in Section X–B.

B. *Stress Model*

The general governing equation for the static-mechanics problem in this Lagrangian frame is given by the force-equilibrium balance in Eq. [3].[44]

$$\nabla\cdot\underset{\approx}{\sigma} + \rho b = \underset{\sim}{0} \qquad [3]$$

Below the meniscus region, axial temperature gradients and the corresponding displacement gradients are generally small, so it is reasonable to apply a generalized plane-strain assumption in the casting direction. This enables a 2-D transient-stress analysis to provide a reasonable approximation of the complete 3-D stress state. Although this is not quite as accurate as a fully 3-D analysis,[31] this slice-model approach can realistically model the entire continuous casting process, with the possible exception of the meniscus region, at a relatively small computational cost.

The incremental governing equations acting over each time step (Δt), for the generalized plane-strain condition, simplify Eq. [3] to the following:

$$\begin{aligned}
\frac{\partial\Delta\sigma_x}{\partial x} + \frac{\partial\Delta\tau_{xy}}{\partial y} &= 0\\
\frac{\partial\Delta\sigma_y}{\partial y} + \frac{\partial\Delta\tau_{xy}}{\partial x} &= 0\\
\int\Delta\sigma_z dA &= \Delta F_z\\
\int x\Delta\sigma_z dA &= \Delta M_x\\
\int y\Delta\sigma_z dA &= \Delta M_y
\end{aligned} \qquad [4]$$

Incremental total strains $\{\Delta\varepsilon\}$ are related to displacements $\{u_x, u_y, u_z\}$ according to Eq. [5].

$$\begin{aligned}
\Delta\varepsilon_x &= \frac{\partial\Delta u_x}{\partial x}\\
\Delta\varepsilon_y &= \frac{\partial\Delta u_y}{\partial y}\\
\Delta\varepsilon_{xy} &= \frac{1}{2}\left(\frac{\partial\Delta u_y}{\partial x} + \frac{\partial\Delta u_x}{\partial y}\right)\\
\Delta\varepsilon_z &= a + bx + cy
\end{aligned} \qquad [5]$$

There are no body forces, because the ferrostatic pressure caused by gravity acting on the liquid is instead applied through the internal boundary conditions described in Section IX–B. Besides the regular boundary conditions like fixed displacements and surface tractions, a special type of boundary, mold-wall constraint, is included in CON2D to model the interactions between the mold wall and the steel surface, as addressed in Section VIII–B. The distorted shape of the mold has an important influence on the size of the interfacial gap, heat transfer, and, consequently, stress, and so is incorporated as discussed in Section VIII–A.

Twofold symmetry can be assumed in the current continuous casting application, so the constants related to bending (b and c in Eq. [5] and ΔM_x and ΔM_y in Eq. [4]) all vanish, and $\Delta\varepsilon_z$ represents the unconstrained axial (thickness) contraction of each 2-D slice.

IV. CONSTITUTIVE MODELS

Increments of stress and elastic strain are related through Hook's Law (Eq. [6]). Matrix $[D]$ contains the isotropic temperature-dependent elastic modulus ($E(T)$), and Poisson's ratio (ν), given in Eq. [7].

$$\{\Delta\sigma\} = [D]\{\Delta\varepsilon_e\} + [\Delta D]\{\varepsilon_e\} \qquad [6]$$

where $\{\sigma\} = \{\sigma_x\ \sigma_y\ \tau_{xy}\ \sigma_z\}^T$ $\{\varepsilon\} = \{\varepsilon_x\ \varepsilon_y\ \varepsilon_{xy}\ \varepsilon_z\}^T$

$$[D] = \frac{E(T)}{(1+\nu)(1-2\nu)}\begin{bmatrix} 1-\nu & \nu & 0 & \nu\\ \nu & 1-\nu & 0 & \nu\\ 0 & 0 & \dfrac{1-2\nu}{2} & 0\\ \nu & \nu & 0 & 1-\nu \end{bmatrix} \qquad [7]$$

The incremental total strains ($\{\Delta\varepsilon\}$) in Eq. [5] are composed of elastic ($\{\Delta\varepsilon_e\}$), thermal, ($\{\Delta\varepsilon_{th}\}$), inelastic ($\{\Delta\varepsilon_{in}\}$), and flow ($\{\Delta\varepsilon_{\text{flow}}\}$) strain components, as given in Eq. [8].

$$\{\Delta\varepsilon\} = \{\Delta\varepsilon_e\} + \{\Delta\varepsilon_{th}\} + \{\Delta\varepsilon_{in}\} + \{\Delta\varepsilon_{\text{flow}}\} \qquad [8]$$

The totals of all strains at a given time ($t + \Delta t$) are obtained by accumulating the strain increments at each prior time step. For example, the total strain is accumulated as follows (Eq. [9]):

$$\{\varepsilon^{t+\Delta t}\} = \{\varepsilon^t\} + \{\Delta\varepsilon^{t+\Delta t}\} \qquad [9]$$

A. *Thermal Strain*

Thermal strains arise due to volume changes caused by both temperature differences and phase transformations, including solidification and solid-state phase changes between crystal structures, such as austenite and ferrite. The isotropic thermal-strain vector, $\{\Delta\varepsilon_{th}\}$, given in Eq. [10], is based on the phase fractions and the thermal linear-expansion function, (TLE), discussed in Section X–C.

$$\left\{\Delta\varepsilon_{th}^{t+\Delta t}\right\} = (\mathrm{TLE}(T^{t+\Delta t}) - \mathrm{TLE}(T^{t}))\left\{1\ 1\ 0\ 1\right\}^{T} \quad [10]$$

B. *Inelastic Strain*

Inelastic strain includes both strain-rate-independent plasticity and time-dependent creep. Creep is significant at the high temperatures of this process and is indistinguishable from plastic strain. Thus, this work adopts a unified constitutive model of the mechanical behavior to capture the temperature- and strain-rate sensitivity of high-temperature steel.

The inelastic strain rate ($\dot{\varepsilon}_{in}$) is described by different constitutive models according to the microstructural state of the solid steel.

$$\dot{\bar{\varepsilon}}_{in} = \begin{cases} \dot{\bar{\varepsilon}}_{in-\delta} & \text{pct } \delta \geq 10 \text{ pct} \\ \dot{\bar{\varepsilon}}_{in-\gamma} & \text{pct } \delta < 10 \text{ pct} \end{cases} \quad [11]$$

where $\dot{\bar{\varepsilon}}_{in-\delta}$ and $\dot{\bar{\varepsilon}}_{in-\gamma}$ are the equivalent inelastic strain rates of ferrite and austenite, respectively, as given in Section X–D. The scalar inelastic strain-rate function follows the ferrite function (δ or α), whenever the phase fraction of ferrite exceeds 10 pct of the total volume. This is justified by considering the steel with two phases to act as a composite material in which only a small amount of the weaker ferrite phase weakens the mechanical strength of the whole material. The plain-carbon steels treated in this work are assumed to harden isotropically, so the von Mises loading surface, associated plasticity, and normality hypothesis in the Prandtl–Reuss flow law is applied:[45]

$$\dot{\underset{\approx}{\varepsilon}}_{in} = \frac{3}{2}\dot{\bar{\varepsilon}}_{in}\frac{\underset{\approx}{\sigma}'}{\bar{\sigma}} \quad [12]$$

where $\dot{\underset{\approx}{\varepsilon}}_{in}$, $\underset{\approx}{\sigma}'$, $\bar{\sigma}$ and $\dot{\bar{\varepsilon}}_{in}$ are the plastic strain-rate tensor, the deviatoric-stress tensor, the equivalent stress scalar (or von Mises effective stress), and equivalent inelastic strain-rate scalar, respectively. In this work, the equivalent inelastic strain rate, $\dot{\bar{\varepsilon}}_{in}$, bears a sign determined by the direction of the maximum principal inelastic strain, as defined in Eq. [13], in order to achieve kinematic behavior (Bauschinger effect) during reverse loading.

$$\dot{\bar{\varepsilon}}_{in} = c\sqrt{\frac{2}{3}\dot{\underset{\approx}{\varepsilon}}_{in} : \dot{\underset{\approx}{\varepsilon}}_{in}}$$

$$\text{where } c = \begin{cases} \dfrac{\varepsilon_{\max}}{|\varepsilon_{\max}|} & \varepsilon_{\max} \geq \varepsilon_{\min} \\ \dfrac{\varepsilon_{\min}}{|\varepsilon_{\min}|} & \varepsilon_{\max} < \varepsilon_{\min} \end{cases} \quad [13]$$

where $\varepsilon_{\max} = \max(\varepsilon_{in11}, \varepsilon_{in22}, \varepsilon_{in33})$ $\varepsilon_{\min} = \min(\varepsilon_{in11}, \varepsilon_{in22}, \varepsilon_{in33})$

The ":" operator indicates standard term-by-term tensor multiplication. Equations [12] and [13] allow an isotropic scalar to represent the 3-D strain-rate state. Appendix B defines $\underset{\approx}{\sigma}'$, $\bar{\sigma}$ and Eq. [12] in 2-D generalized plane-strain form. Parameter c (+1 or −1) makes the equivalent inelastic strain rate have the same sign as the maximum principal inelastic strain. The functions for the inelastic strain-rate scalars, $\dot{\bar{\varepsilon}}_{in}$, described in Section X–D, must be integrated to find the $\{\Delta\varepsilon_{in}\}$ value needed in Eq. [8], as described previously in this section.

C. *Strain in Liquid Elements*

In this model, the liquid elements are generally given no special treatment regarding material properties and finite-element assembly. However, liquid reacts very differently from solid under external loads. It deforms elastically under hydrostatic force like a solid, but deforms dramatically under shear force. If any liquid is present in a given finite element, a constitutive equation is used to generate an extremely rapid creep (shear) rate:

$$\dot{\bar{\varepsilon}}_{\mathrm{flow}} = \begin{cases} cA\left(|c\bar{\sigma}| - \sigma_{\mathrm{yield}}\right) & |c\bar{\sigma}| > \sigma_{\mathrm{yield}} \\ 0 & |c\bar{\sigma}| \leq \sigma_{\mathrm{yield}} \end{cases} \quad [14]$$

The parameter A is chosen to be 1.5×10^8 $\mathrm{MPa}^{-1}\mathrm{s}^{-1}$ to match the viscosity of molten steel.[46] Equation [14] is another format of the linear viscous equation[43] of the laminar fluid, which is a reasonable assumption for the liquid steel in the mushy zone. Liquid deforms under any nonzero shear stress according to Newtonian fluid dynamics. Thus, σ_{yield} should be zero. To avoid numerical difficulty, however, σ_{yield} is treated as a tolerance-accuracy parameter with no physical nature and is given a value of 0.01 MPa.

This method effectively increases shear strain and, thus, enforces negligible liquid strength and shear stress. The critical temperature where the liquid fraction is sufficient to make the element act as a liquid is the "coherency temperature" ($T_{\mathrm{coherency}}$), currently defined as being equal to the solidus temperature. To generalize this scalar strain rate to a multidimensional strain vector, the same Prandtl–Reuss Eqs. [12] and [13] are used as for the solid, $\dot{\bar{\varepsilon}}_{in}$.

This fixed-grid approach avoids the difficulties of adaptive meshing while allowing strain to accumulate in the mushy region. As in the real continuous casting process, the total mass of the liquid domain is not constant. The inelastic strain accumulated in the liquid represents mass transport due to fluid flow and, so, is denoted "flow strain." Positive flow strain indicates fluid feeding into the region. This is important for the prediction of hot-tear cracks. The disadvantage of using this high-creep-rate function to model liquid is the increased computational difficulty at the solidification front. This requires the use of a very robust local iteration algorithm.[3]

V. FINITE-ELEMENT IMPLEMENTATION

A. *Heat-Transfer and Solidification Model*

The three-node triangle finite element was employed to approximate temperature in the domain as a piecewise linear function. The standard Galerkin method[44] applied to Eq. [2] gives the following global matrix equations:

$$[K]\{T\} + [C]\{\dot{T}\} = \{F_q\} + \{F_{\mathrm{qsup}}\} \quad [15]$$

where $[K]$ is the conductance matrix including the effect of conductivity ($k(T)$), and $[C]$ is the capacitance matrix including the effect of specific heat and latent heat in $H(T)$. Within each element, an effective specific heat (c_{pe}) is evaluated using a spatial averaging technique suggested by Lemmon.[47]

$$c_{pe} = \frac{\partial H}{\partial T} = \sqrt{\frac{\left(\frac{\partial H}{\partial x}\right)^2 + \left(\frac{\partial H}{\partial y}\right)^2}{\left(\frac{\partial T}{\partial x}\right)^2 + \left(\frac{\partial T}{\partial y}\right)^2}} \qquad [16]$$

The $[K]$ and $[C]$ matrices are found from their element matrices, given in Appendix A, through standard finite-element method summation over the domain. A three-level time-stepping method proposed by Dupont *et al.*[48] was adopted to solve Eq. [15]. Temperatures at the current time $t + \Delta t$ are found from the temperatures at the previous two time steps, t and $t - \Delta t$.

$$\{T\} = \frac{1}{4}\left\{3T^{t+\Delta t} + T^{t-\Delta t}\right\} \qquad [17]$$

$$\{\dot{T}\} = \left\{\frac{T^{t+\Delta t} - T^{t}}{\Delta t}\right\} \qquad [18]$$

Substituting Eqs. [17] and [18] into Eq. [15] and rearranging gives a recursive global matrix equation expressing the time and spatial discretization of the heat-conduction equation (Eq. [2]).

$$\left[\frac{3}{4}[K] + \frac{[C]}{\Delta t}\right]\{T^{t+\Delta t}\} = \{F_q\} + \{F_{\text{qsup}}\} - \frac{1}{4}[K]\left\{T^{t-\Delta t}\right\} + \frac{[C]}{\Delta t}\{T^{t}\} \qquad [19]$$

Equation [19] is solved at each time step for the unknown nodal temperatures $\{T^{t+\Delta t}\}$ using a Choleski decomposition solver.[49] The terms $\{F_q\}$ and $\{F_{\text{qsup}}\}$ are the heat-flow-load vectors containing the distributed heat flux at the domain boundary and the superheat flux at the internal moving boundary, respectively. On each domain boundary where heat flux is applied, the contributions from each element on the boundary are summed as follows:

$$\{F_q\} = \sum_{\text{boundary elements}} \int [N]^T q \, dL = \sum_{\text{boundary elements}} \begin{Bmatrix} \frac{q_{ij} L_{ij}}{2} \\ \frac{q_{ij} L_{ij}}{2} \end{Bmatrix} \qquad [20]$$

where L_{ij} is the distance between node i and j. The heat-flux function (q) is specified, such as being equal to the q_{gap} value given in Section VII. The term $\{F_{\text{qsup}}\}$ is calculated similarly with a different set of boundary elements, using q_{sup} in Section VII.

B. *Stress Model*

Applying the standard Galerkin method to Eqs. [4] through [7] gives the following set of linear equations over the finite-element domain:

$$[K]\{\Delta u\}^{t+\Delta t} = \{\Delta F_{th}\}^{t+\Delta t} + \{\Delta F_{in}\}^{t+\Delta t} + \left\{F_{fp}\right\}^{t+\Delta t} - \{F_{el}\}^{t} \qquad [21]$$

where $[K]$, $\{\Delta F_{th}\}$, $\{\Delta F_{in}\}$, $\{F_{fp}\}$, and $\{F_{el}\}$ are the stiffness matrix and incremental force vectors due to incremental thermal strain, inelastic strain, ferrostatic pressure and external surface tractions at specified boundaries, and elastic-strain corrections from the previous time step, respectively. Refer to Eqs. [64] through [67] in Appendix B for more details. At each time step, Eq. [21] is solved for the incremental displacements ($\{\Delta u\}$) using the Choleski method,[49] and the total displacements are updated *via* Eq. [22].

$$\{u\}^{t+\Delta t} = \{u\}^{t} + \{\Delta u\} \qquad [22]$$

Then, the total strains and stresses are updated from Eqs. [5] and [6], respectively. The six-node quadratic-displacement triangle elements use the same grid of nodes that were connected into three-node elements for the heat-flow calculation. Further details are given in Appendix B.

VI. INTEGRATION OF THE CONSTITUTIVE MODEL

Highly strain-rate-dependent inelastic models require a robust numerical integration technique to avoid numerical difficulties. The nonlinear equations to be integrated are given in Eqs. [23] and [24] by combining Eqs. [6] through [8], neglecting the second term on the right-hand side of Eq. [6].

$$\underset{\approx}{\sigma}^{t+\Delta t} = \underset{\approx}{D}^{t+\Delta t} : \left(\underset{\approx}{\varepsilon}^{t} - \underset{\approx}{\varepsilon}^{t}_{th} - \underset{\approx}{\varepsilon}^{t}_{in} + \Delta \underset{\approx}{\varepsilon}^{t+\Delta t} - \Delta \underset{\approx}{\varepsilon}^{t+\Delta t}_{th} - \Delta \underset{\approx}{\varepsilon}^{t+\Delta t}_{in}\right) \qquad [23]$$

$$\bar{\varepsilon}^{t+\Delta t}_{in} = \bar{\varepsilon}^{t}_{in} + \Delta \bar{\varepsilon}^{t+\Delta t}_{in} \qquad [24]$$

The incremental equivalent plastic strain accumulated over a time step is given in Eq. [25] based on a highly nonlinear constitutive function, which depends on $\bar{\sigma}$ and $\bar{\varepsilon}_{in}$, which change greatly over the time step.

$$\Delta \bar{\varepsilon}^{t+\Delta t}_{in} = F(T, \bar{\sigma}^{t+\Delta t}, \bar{\varepsilon}^{t+\Delta t}_{in}, \text{pct C})\Delta \text{t} \qquad [25]$$

where F is one of the constitutive functions given in Eqs. [46], [47], or [14], depending on the current material state. Substituting Eqs. [12] and [25] into Eqs. [23] and [24] and using a fully implicit time-stepping method, a new set of evolution equations are obtained as follows:

$$\underset{\approx}{\sigma}^{t+\Delta t} = \underset{\approx}{D}^{t+\Delta t} : \left(\underset{\approx}{\varepsilon}^{t} - \underset{\approx}{\varepsilon}^{t}_{th} - \underset{\approx}{\varepsilon}^{t}_{in} + \Delta \underset{\approx}{\hat{\varepsilon}} - \dot{\underset{\approx}{\varepsilon}}^{t+\Delta t}_{th} \Delta t - \frac{3}{2} F(T, \bar{\sigma}^{t+\Delta t}, \bar{\varepsilon}^{t+\Delta t}_{in}, \text{pct C}) \frac{\underset{\approx}{\sigma}^{t+\Delta t\prime}}{\bar{\sigma}^{t+\Delta t}} \Delta t\right) \qquad [26]$$

$$\bar{\varepsilon}^{t+\Delta t}_{in} = \bar{\varepsilon}^{t}_{in} + F(T, \bar{\sigma}^{t+\Delta t}, \bar{\varepsilon}^{t+\Delta t}_{in}, \text{pct C})\Delta t \qquad [27]$$

Two tensors, $\underset{\approx}{\sigma}^{t+\Delta t}$ and $\Delta \underset{\approx}{\hat{\varepsilon}}$, and one scalar, $\bar{\varepsilon}^{t+\Delta t}_{in}$, comprise 13 unknown scalar fields for 3-D problems or nine unknowns for the 2-D problem here, which require the solution of Eqs. [26] and [27]. Zhu implemented an alternating implicit-explicit mixed time-integration scheme, which is based on an operator-splitting technique that alternates between local and global forms of the total strain increment and inelastic strain rate over each pair of successive steps.[3] Within each time step, $\underset{\approx}{\sigma}^{t+\Delta t}$ and $\bar{\varepsilon}^{t+\Delta t}_{in}$ are first solved

using a fully implicit time-integration technique based on the current best estimation of the total strain increment $\Delta\hat{\underset{\approx}{\varepsilon}}$, which is taken from the previous time step $\Delta\underset{\approx}{\varepsilon}^t$. This is a "local step" because it is spatially uncoupled.

Then, the improved estimates of $\underset{\approx}{\sigma}^{t+\Delta t}$ and $\bar{\varepsilon}_{in}^{t+\Delta t}$ from the local step are used to solve for $\Delta\underset{\approx}{\varepsilon}$ by explicit finite-element spatial integration through Eqs. [21] and [5]. This is a "global step."[3]

There is still a tensor unknown in Eq. [26], which makes even the local time-integration step computationally challenging. Lush *et al*. transformed this tensor equation into a scalar equation for isotropic materials with isotropic hardening.[50]

$$\bar{\sigma}^{t+\Delta t} = \bar{\sigma}^{*t+\Delta t} - 3\mu^{t+\Delta t} F(T, \bar{\sigma}^{t+\Delta t}, \bar{\varepsilon}_{in}^{t+\Delta t}, \text{pct C})\Delta t \quad [28]$$

where $\bar{\sigma}^{*t+\Delta t}$ is the equivalent stress of the stress tensor, $\underset{\approx}{\sigma}^{*t+\Delta t}$, defined subsequently.

$$\underset{\approx}{\sigma}^{*t+\Delta t} = \underset{\approx}{D}^{t+\Delta t} : (\underset{\approx}{\varepsilon}^t - \underset{\approx}{\varepsilon}_{th}^t - \underset{\approx}{\varepsilon}_{in}^t + \Delta\hat{\underset{\approx}{\varepsilon}} - \dot{\underset{\approx}{\varepsilon}}_{th}^{t+\Delta t}\Delta t \quad [29]$$

Equations [27] and [28] form a pair of nonlinear scalar equations to solve in the local step for estimates of the two unknowns $\bar{\varepsilon}_{in}^{t+\Delta t}$ and $\bar{\sigma}^{t+\Delta t}$.

Stress-Model Numerical Integration Procedure

Implementing the general 3-D procedure described previously for the 2-D generalized plane-strain assumption, the integration procedure used in CON2D within each time step is summarized as follows.

(1) Estimate $\{\Delta\hat{\varepsilon}\}$ based on $\{\Delta u\}$ from the previous time step: $\{\Delta\hat{\varepsilon}\} = [B]\{\Delta u\}^t$.
(2) Calculate $\{\sigma^*\}^{t+\Delta t}$, $\bar{\sigma}^*$, and $\{\sigma^{*\prime}\}^{t+\Delta t}$, needed to define the direction of the stress vector.

$$\{\sigma^*\}^{t+\Delta t} = [D]^{t+\Delta t}\big(\{\varepsilon\}^t - \{\varepsilon_{th}\}^t - \{\varepsilon_{in}\}^t + \{\Delta\hat{\varepsilon}\} - \dot{\varepsilon}_{th}^{t+\Delta t}\Delta t\{1\ 1\ 0\ 1\}^T\big) \quad [30]$$

(3) Solve the following two ordinary differential equations simultaneously for $\bar{\varepsilon}_{in}^{t+\Delta t}$ and $\bar{\hat{\sigma}}^{t+\Delta t}$ at each local Gauss point, using a fully implicit bounded Newton–Raphson integration method from Lush et al.[50] This method gives the best robustness and efficiency of several alternative approaches evaluated.[3] Function F is either the Kozlowski model III for γ (Eq. [46]), the power law for δ (Eq. [47]), or the flow strain for liquid phase (Eq. [14]).

$$\begin{aligned}\bar{\varepsilon}_{in}^{t+\Delta t} &= \bar{\varepsilon}_{in}^t + F(T, \bar{\hat{\sigma}}^{t+\Delta t}, \bar{\varepsilon}_{in}^{t+\Delta t}, \text{pct } C)\Delta t \\ \bar{\hat{\sigma}}^{t+\Delta t} &= \bar{\sigma}^{*t+\Delta t} - 3\mu^{t+\Delta t} F(T, \bar{\hat{\sigma}}^{t+\Delta t}, \bar{\varepsilon}_{in}^{t+\Delta t}, \text{pct } C)\Delta t\end{aligned} \quad [31]$$

(4) Expand this scalar stress estimate into vector form:*

$$\{\sigma^{*\prime}\}^{t+\Delta t} = \{\sigma^*\}^{t+\Delta t} - \frac{1}{3}\sigma_m^{*t+\Delta t}\{\delta\}^T;\ \sigma_m^{*t+\Delta t} = \sigma_x^{*t+\Delta t} + \sigma_y^{*t+\Delta t} + \sigma_z^{*t+\Delta t};\ \{\delta\} = \{1\ 1\ 0\ 1\}$$

$$\{\hat{\sigma}\}^{t+\Delta t} = \bar{\hat{\sigma}}^{t+\Delta t}\frac{\{\sigma^{*\prime}\}^{t+\Delta t}}{\bar{\sigma}^{*t+\Delta t}} + \frac{1}{3}\sigma_m^{*t+\Delta t}\{\delta\}^T \quad [32]$$

(5) Calculate $\dot{\bar{\varepsilon}}_{in}^{t+\Delta t}$ from $\bar{\hat{\sigma}}^{t+\Delta t}$ and $\bar{\varepsilon}_{in}^{t+\Delta t}$ using the appropriate F values for the local material phase.
(6) Expand this scalar inelastic-strain estimate into a vector $\{\dot{\varepsilon}_{in}\}^{t+\Delta t}$ with the same direction as $\{\hat{\sigma}'\}^{t+\Delta t}$ using the Prandtl–Reuss Eq. [12]; update $\{\varepsilon_{in}\}^{t+\Delta t} = \{\varepsilon_{in}\}^t + \{\dot{\varepsilon}_{in}\}^{t+\Delta t}\Delta t$ only for solidified elements.
(7) Use classic finite-element method spatial integration (Appendix B) to solve Eq. [21] for $\{\Delta u\}^{t+\Delta t}$ based on $\{\dot{\varepsilon}_{in}\}^{t+\Delta t}$.
(8) Finally, find $\{\Delta\varepsilon\}^{t+\Delta t}$ from $\{\Delta u\}^{t+\Delta t}$ and update $\{\varepsilon\}^{t+\Delta t}$ and $\{\sigma\}^{t+\Delta t}$.

Overall, this alternating implicit-explicit scheme with the bounded Newton–Raphson iteration gives the best robustness and efficiency of several alternative finite-element method time-integration approaches evaluated.[3]

VII. TREATMENT OF THE MOLD/SHELL INTERFACE

Heat transfer does not depend directly on the force-equilibrium equation, because the mechanical dissipation energy is negligible. The heat-flow and stress models are fully coupled with each other, however, when the gap between the mold and steel shell is taken into account. Shrinkage of the shell tends to increase the thermal resistance across the gap where the shell is strong enough to pull away from the mold wall. This leads to hot and weak spots on the shell. This interdependence of the gap size and the thermal resistance requires iteration between the heat-a priori and stress models. As the gap size is unknown advance, the heat resistance is also unknown. Thus, iterations within a time step are usually needed. Contact between the mold wall and shell surface is discussed in Section VIII–B.

A. *Interface Heat Transfer*

When the coupled heat-transfer and thermal-stress analysis is performed, the heat-transfer boundary condition at the steel surface is described by a gap heat-resistor model shown in Figure 2, with parameter values listed in Table I. Heat leaves

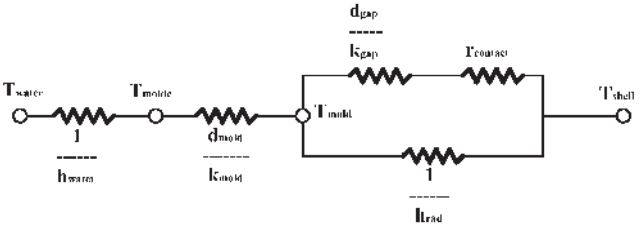

Fig. 2—Schematic of thermal resistor model of the interfacial layer between mold and billet

Table I. Parameters of the Interface Model

Cooling water heat-transfer coefficient, h_{water} (W/m^2 K)	22,000 to 25,000
Cooling water temperature, T_{water} (°C)	30 to 42
Mold wall thickness, d_{mold} (mm)	6
Mold wall conductivity, k_{mold} (W/m K)	360
Gap conductivity, k_{gap} (W/m K)	0.02
Contact resistance, $r_{contact}$ (m^2 K/W)	6×10^{-4}
Mold wall emissitivity	0.5
Steel emissitivity	0.8

the steel shell *via* conduction and radiation across the interfacial gap. It is then conducted across the thin copper mold and extracted by cooling water flowing across the back of the mold tube. The temperature and the heat-convection coefficient of the cooling water are input from the results of a preliminary computation using the CON1D model, described elsewhere.[51] The contact resistance adopted in this model is several orders of magnitude larger than the physical contact resistance[46] between a flat steel and copper surface, because it includes the influence of oscillation marks.[51] The gap thickness is calculated during each iteration from the shell-surface displacement and the mold wall position, according to the local values of the mold taper and distortion, which are described in the next section. Once the gap size is determined, the heat flux (q_{gap}) across the interfacial layer between the mold wall and steel surface is solved together with the mold hot-face temperature (T_{mold}):

$$q_{gap} = \frac{T_{shell} - T_{water}}{r_{gapmold}} \quad [33]$$

where

$$r_{gapmold} = \frac{1}{h_{water}} + \frac{T_{mold}}{k_{mold}} + \frac{\frac{d_{gap}}{k_{gap}} + r_{contact}}{1 + h_{rad}\left(\frac{d_{gap}}{k_{gap}} + r_{contact}\right)}$$

$$h_{rad} = 5.67 \times 10^{-8} \bar{e}(T_{shell} + T_{mold})(T_{shell}^2 + T_{mold}^2)$$

$$\bar{e} = \frac{1}{\frac{1}{\varepsilon_m} + \frac{1}{\varepsilon_s} + 1}$$

$$T_{mold} = \frac{5.67 \times 10^{-8} \bar{e}\, T_{shell}^4 + T_{shell}/r_{mold} + T_{water}/r_{gap}}{1/r_{mold} + 1/r_{gap}}$$

$$r_{mold} = \frac{d_{mold} h_{water} + k_{mold}}{h_{water} k_{mold}}$$

$$r_{gap} = \frac{d_{gap}}{k_{gap}} + r_{contact}$$

B. *Gap-Size Calculation*

The gap thickness (d_{gap}) is estimated for each boundary node at the shell surface, based on gaps from the previous iteration (n):

$$\hat{d}_{gap}^{n+1} = \max\left(\{u(d_{gap}^n)\} \times \hat{n} - d_{wall}^{t+\Delta t}, d_{gapmin}\right)$$

where [34]

$$d_{wall}^{t+\Delta t} = d_{taper}^{t+\Delta t} - d_{molddist}^{t+\Delta t}$$

where $\{u\}$, $\hat{n}$, d_{wall}, d_{taper}, $d_{molddist}$, and d_{gapmin} are the displacement vector at boundary nodes, unit-normal vector to the mold wall surface, mold wall position, mold wall position change due to mold distortion, and the minimum gap thickness, respectively. A positive d_{gap} value indicates a real space between the mold and shell.

The minimum gap value is set as

$$d_{gapmin} = r_{contact} k_{gap} \quad [35]$$

It physically represents the effective oscillation-mark depth at the shell surface. When the calculated gap size is less than this minimum gap size, then the contact resistance ($r_{contact}$) dominates heat transfer between the shell surface and the mold wall. Gap-size variation within the minimum gap size is assumed not to affect the thermal resistance, which accelerates convergence.

C. *Thermal-Stress Coupling*

The overall flow of CON2D is shown in Figure 3. Within each time step, the computation alternates between the heat-transfer and stress models through the following fully coupled procedure

(1) The temperature field is solved based on the current best estimation of gap size, from the previous time step, with Eq. [34]. The initial gap size at the beginning of the simulation is simply zero around the strand perimeter as the liquid steel at the meniscus flows to match the mold contour.
(2) The incremental thermal strain is evaluated from the temperature field at the current and previous time steps (Eq. [10]). The inelastic strain is estimated by integrating Eq. [31] following the procedure described in Section VI. The global matrix equation, Eq. [21], is solved for displacements, strains, and stresses using the standard finite-element method.
(3) The gap sizes for the next iteration are updated by

$$d_{gap}^{n+1} = \beta \hat{d}_{gap}^{n+1} + (1 - \beta) d_{gap}^n \quad [36]$$

where β is chosen to be 0.5.
(4) Finally, steps 1 through 3 are repeated until the gap-size difference between two successive heat-transfer and stress iterations, n and $n + 1$, is small enough:

$$d_{diff} = \sqrt{\frac{\sum_{nb}\left(d_{gap}^{n+1} - d_{gap}^n\right)^2}{\sum_{nb}\left(d_{gap}^{n+1}\right)^2}} \quad [37]$$

where nb is the number of boundary nodes. When d_{diff} becomes smaller than the specified "gap tolerance" (d_{min}), the gap size is considered converged.

VIII. MODELING THE MOLD WALL

The mold wall affects the calculation in two ways: (1) altering the size of the interfacial gap and associated heat transfer between the mold and strand through its distorted shape; and (2) constraining the shell from bulging due to the internal ferrostatic pressure.

A. *Mold Wall Shape*

The mold wall is defined in CON2D as a function of distance below the meniscus. The shape of the mold varies from its dimensions at the meniscus due to mold taper and mold distortion. The mold is tapered to follow the shrinkage of the steel strand to prevent excessive gaps from forming between the mold wall and shell surface, as well as

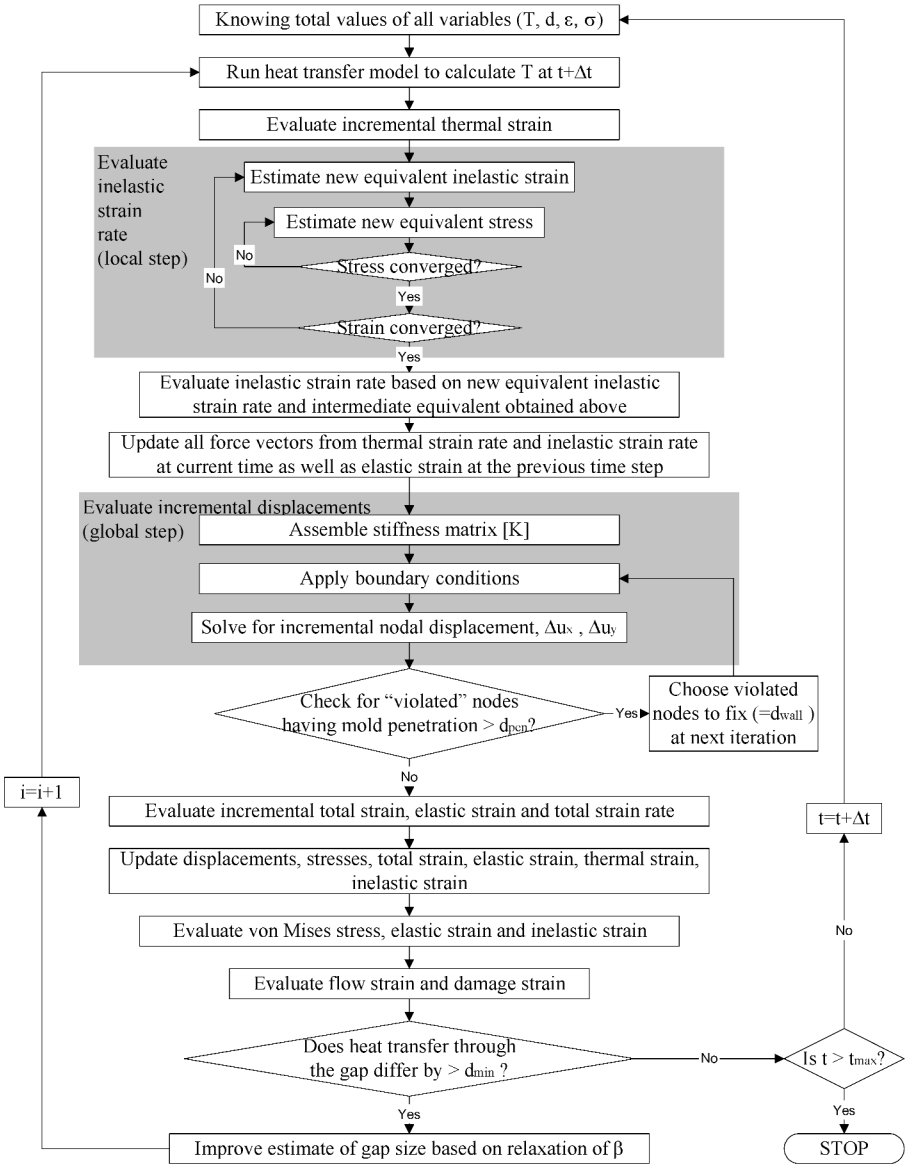

Fig. 3—Flow chart of CON2D.

preventing bulging of the shell. Linear taper is defined by providing the percentage per meter as follows:

$$d_{\text{taper}} = \frac{\text{pct Taper/m}}{100} \frac{W}{2} v_c t \qquad [38]$$

where W, v_c, and t are the mold width, casting speed, and current time below the meniscus, respectively. As the modeled section of the steel strand moves down from the meniscus, the mold wall distorts away from the solidifying shell and tapers toward it.

Mold distortion arises from two main sources: thermal expansion of the mold wall due to heating during operation, and mold wear due to friction between the mold and the strand. For the billet-casting simulation presented here, mold distortion is considered to be simple thermal expansion as follows, ignoring residual distortion and mold wear.

$$d_{\text{molddist}} = \alpha_{\text{mold}} \frac{W}{2} \left(\overline{T} - \overline{T}_0 \right) \qquad [39]$$

where $\overline{T}$ is the average temperature through the mold wall thickness as a function of the distance below the mold exit, $\overline{T}_0$ is the average mold wall temperature where the solid shell begins at the meniscus, α_{mold} is the thermal-expansion coefficient of the copper mold tube, and W is the section width.

Arbitrary complex mold shapes can be modeled by providing an external data file or function with mold wall positions at different distances below the meniscus and even around the perimeter. For example, complex 3-D mold distortion profiles[52] were used for slab casting simulations with CON2D.[2,6]

B. *Contact Algorithm for Shell-Surface Constraint*

The mold wall provides support to the solidifying shell before it reaches the mold exit. A proper mold wall constraint is needed to prevent the solidifying shell from penetrating the mold wall, while also allowing the shell to shrink freely. Because the exact contact area between the mold wall and the solidifying shell is not known *a priori*, an iterative solution procedure is needed.

Some early finite-element models solved contact problems by the Lagrange multiplier approach, which introduces new unknowns to the system as well as numerical difficulties.[53] This work adopts a method developed and implemented by Moitra,[2,6] which is tailored to this particular casting-problem domain. It solves the contact problem only approximately, but is easy to implement and is more stable. Iteration within a time step proceeds as follows.

At first, the shell is allowed to deform freely without mold constraint. Then, the intermediate shell surface is compared to the current mold wall position. A fraction of all penetrating nodes, identified by Eq. [40], is restrained back to the mold wall position by a standard penalty method, and the stress simulation is repeated.

$$\{u\} \cdot \hat{n} - d_{\text{wall}} < -d_{\text{pen}} \qquad [40]$$

where d_{pen} is the specified penetration tolerance. Iteration continues until no penetration occurs.

The nodes to be constrained are chosen by checking three scenarios.

(1) In Figure 4(a), a portion of the shell surface with length L penetrates the mold, and the maximum penetration is found at the centerline of the strand face. Those shell boundary nodes in the half of this violated length nearest to the face center (L_c) are constrained in the next iteration.
(2) In Figure 4(b), the center of the shell surface penetrates the mold but does not penetrate the most. Those violated nodes from the maximum penetration position to the face center are constrained in the next iteration.
(3) In Figure 4(c), the center of the shell surface does not penetrate the mold. That half of the violated nodes closest to the face center is constrained in the next iteration.

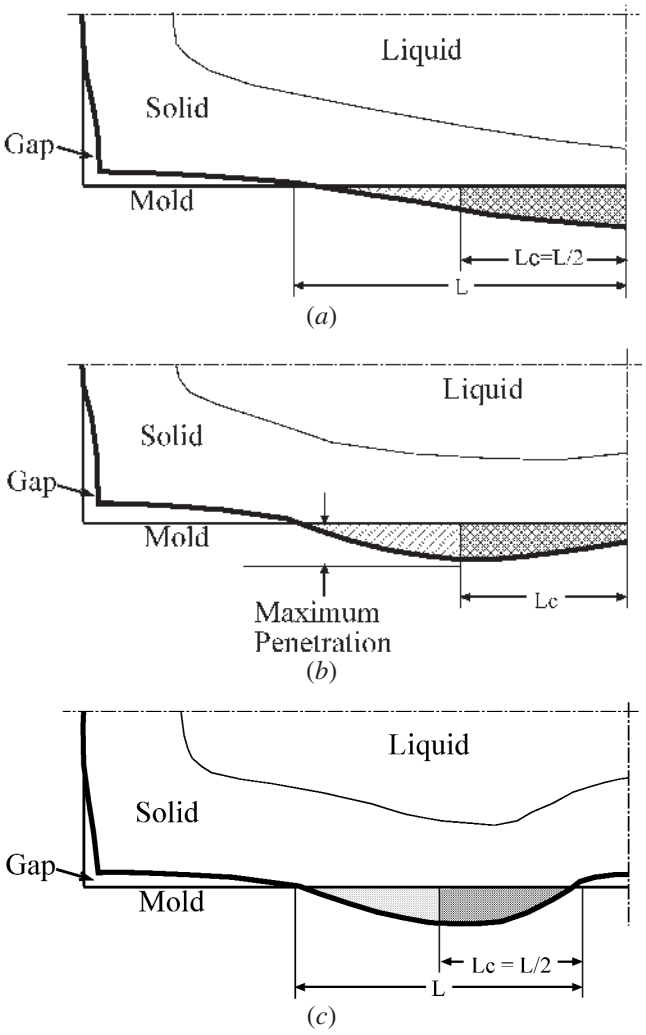

Fig. 4—(*a*) through (*c*) Three types of penetration modes in contact algorithm.

Commercial software, such as ABAQUS, generally constrains violated nodes one by one until convergence is reached. The present method is believed to be more computationally efficient for the particular quarter mold and behavior of interest in this work. The friction between the shell and mold surface is ignored in this model. This would need to be added to consider phenomena such as transverse cracks due to excessive taper.

IX. SOLIDIFICATION FRONT TREATMENT

A. *Superheat Flux*

Superheat is the amount of heat stored in the liquid steel that needs to be extracted before it reaches the liquidus temperature. Superheat is treated in one of two ways: (1) the heat-conduction method and (2) the superheat-flux method. The heat-conduction method simply sets the initial steel temperature to the pouring temperature and increases the conductivity of the liquid by 6.5 times to crudely approximate the effects of fluid flow. This method equally distributes the superheat over the solidification front. In reality, the superheat distribution is uneven due to the flow pattern in the liquid pool.

The second method first obtains the superheat-flux distribution from a separate fluid-flow computation, such as done previously for billets[54] or slabs.[55] This superheat flux at a given location on the strand perimeter is applied to appropriate nodes on the solidification front. Specifically, it is applied to the two nodes just below the liquidus in those 3-node elements with exactly one node above the liquidus. This is shown in Figure 5, where the isotherm is the liquidus. The initial liquid temperature is set just above the liquidus, to avoid accounting for the superheat twice.

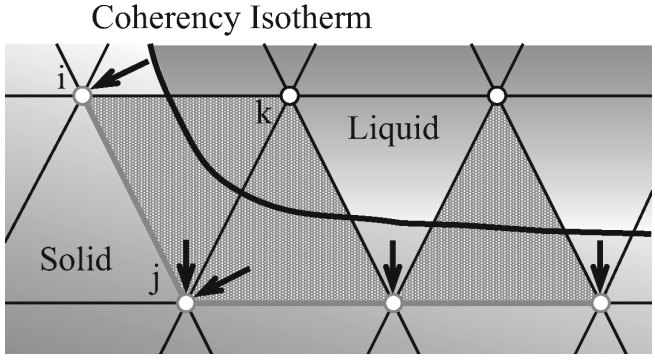

Fig. 5—Schematic of how ferrostatic pressure is applied at the internal boundary.

B. *Ferrostatic Pressure*

Ferrostatic pressure greatly affects gap formation by encouraging contact between the shell and mold, depending on the shell strength. The ferrostatic pressure is calculated by

$$F_p = \rho g z \qquad [41]$$

where z is the distance of the current slice from the meniscus, found from the casting speed and the current time. Ferrostatic pressure is treated as an internal load that pushes the shell toward the mold wall, as shown in Figure 5. It is applied equally to those two nodes just below the coherency temperature that belong to those three-node elements having exactly one of its three nodes above the $T_{\text{coherency}}$ isotherm. It is assembled to the global force vector through Eq. [64] in Appendix B, which gives

$$\{F_{fp}\} = \sum_{\text{moving}} \sum_{\text{boundary}} \sum_{\text{elements}} \begin{Bmatrix} \frac{F_p L_{ij}}{2} \\ \frac{F_p L_{ij}}{2} \end{Bmatrix} \qquad [42]$$

where L_{ij} is the boundary length between nodes i and j within a three-node element.

X. MATERIAL PROPERTIES

This work adopts temperature-dependent steel properties chosen to be as realistic as possible.

A. *Phase-Fraction Model*

A pseudobinary-phase diagram for certain plain-carbon steels,* developed from measurements by WON,[56] is incorporated to produce realistic phase-fraction evolution between the solidus and liquidus temperatures. Figure 6 shows the nonequilibrium Fe-C phase diagram, which defines the volume fractions of liquid, δ-ferrite, and austenite used in this work. The classical lever rule is used to calculate phase fractions in each two-phase region, and a lever rule for ternary systems is used in the three-phase region.[57] The 100 and 75 pct solid lines are compared with zero strength temperature (ZST) and zero ductility temperature (ZDT) measurements by Schmidtmann *et al.*[38] They match very well.

Figure 7 shows the phase fractions thus generated as a function of temperature for the 0.04 pct C carbon steel, which is used in Section XIII. Note that the liquid fraction decreases parabolically as the steel cools from its liquidus. This agrees with a more sophisticated microsegregation model.[38]

B. *Thermal Properties*

The temperature-dependent conductivity function for plain-carbon steel is fitted from measured data compiled by Harste[58] and is given in Eq. [43]. Figure 8 shows the conductivity for several typical plain-carbon steels. The conductivity increases linearly through the mushy zone to the liquid by a factor of 6.5 to partly account for the effect of convection due to flow in the liquid steel pool.[55]

$$K(\text{W/mK}) = K_\alpha f_\alpha + K_\gamma f_\gamma + K_\delta f_\delta + K_l f_l$$

where

$$K_\alpha = (80.91 - 9.9269 \times 10^{-2} T(^\circ\text{C}) + 4.613 \times 10^{-5} T(^\circ\text{C})^2)\,(1 - a_1(\text{pct C})^{a_2})$$

*Other elements besides iron and carbon are 1.52 wt pct Mn, 0.015 wt pct S, 0.012 wt pct P, and 0.34 wt pct Si.

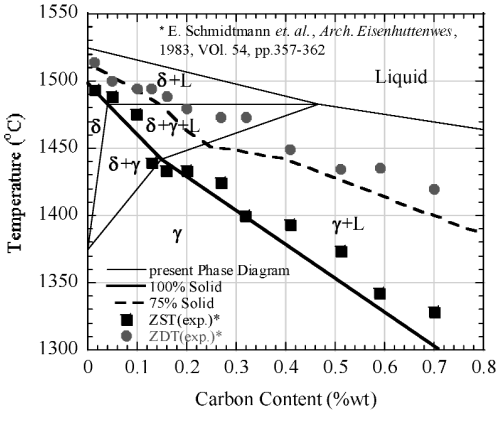

Fig. 6—Non-equilibrium Fe-C phase diagram[38] used in CON2D.

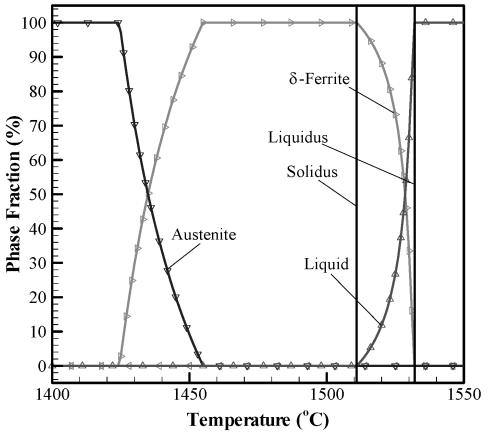

Fig. 7—Fraction as a function of temperature for the 0.04%C steel.

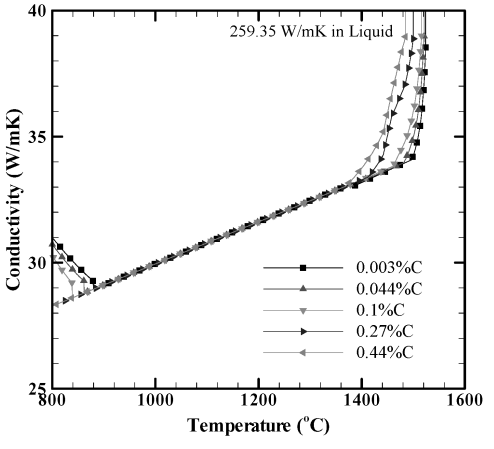

Fig. 8—Conductivity of plain carbon steels.

$$K_\gamma = 21.6 - 8.35 \times 10^{-3} T(^\circ\mathrm{C}) \quad [43]$$

$$K_\delta = (20.14 - 9.313 \times 10^{-3} T(^\circ\mathrm{C}))(1 - a_1(\text{pct C})^{a_2})$$

$$K_l = 39.0$$

$$a_1 = 0.425 - 4.385 \times 10^{-4} T(^\circ\mathrm{C})$$

$$a_2 = 0.209 + 1.09 \times 10^{-3} T(^\circ\mathrm{C})$$

The enthalpy curve used to relate heat content and temperature in this work, $H(T)$, is obtained by integrating the specific heat curve fitted from measured data complied by Harste[58] as given in Eq. [44]. Figure 9 shows the enthalpy for typical plain-carbon steels.

$$H(\mathrm{kJ/Kg}) = H_\alpha f_\alpha + H_\gamma f_\gamma + H_\delta f_\delta + H_l f_l$$

where

$$H_\alpha = \begin{cases} 5188\ T(\mathrm{K})^{-1} - 86 + 0.505T(\mathrm{K}) \\ \quad - 6.55 \times 10^{-5}\ T(\mathrm{K})^2 + 1.5 \times 10^{-7}\ T(\mathrm{K})^3 & T(\mathrm{K}) \le 800 \\ \quad - 1.11 \times 10^6\ T(\mathrm{K})^{-1} - 4.72\ T(\mathrm{K}) & \\ \quad + 2.292 \times 10^{-3}\ T(\mathrm{K})^2 + 4056 & 800 < T(\mathrm{K}) \le 1000 \\ \quad - 11.5\ T(\mathrm{K}) + 6.238 \times 10^{-3}\ T(\mathrm{K})^2 & \\ \quad + 5780 & 1000 < T(\mathrm{K}) \le 1042 \\ 34.87\ T(\mathrm{K}) - 0.016013\ T(\mathrm{K})^2 & \\ \quad - 18{,}379 & 1042 < T(\mathrm{K}) \le 1060 \\ \quad - 10.068\ T(\mathrm{K}) + 2.9934 \times 10^{-3}\ T(\mathrm{K})^2 & \\ \quad - 5.21766 \times 10^6\ T(\mathrm{K})^{-1} + 12{,}822 & 1060 < T(\mathrm{K}) \le 1184 \end{cases}$$

$$H_\gamma = 0.43T(\mathrm{K}) + 7.5 \times 10^{-5} T(\mathrm{K})^2 + 93 + a_\gamma$$

$$\text{where } a_\gamma = \frac{[37(\text{pct C}) + 1.9 \times 10^3(\text{pct C})^2]}{(44(\text{pct C}) + 1200)}$$

$$H_\delta = 0.441T(\mathrm{K}) + 8.87 \times 10^{-5} T(\mathrm{K})^2 + 51 + a_\delta$$

$$\text{where } a_\delta = \frac{[18(\text{pct C}) + 2.0 \times 10^3(\text{pct C})^2]}{(44(\text{pct C}) + 1200)}$$

$$H_l = 0.825T(\mathrm{K}) - 105 \quad [44]$$

For the multiphase region, both conductivity and enthalpy are calculated by weighted averaging of their different phase fractions (f). The subscripts (α, γ, δ, and l) in Eqs. [43] and [44] represent α-ferrite, austenite, δ-ferrite, and liquid, respectively. Density is assumed constant (7400 Kg/m^3) in order to maintain constant mass.

C. *Thermal Linear Expansion*

The thermal linear-expansion function is obtained from solid-phase density measurements complied by Harste[58] and Harste *et al.*[59] and liquid density measurements by Jimbo and Cramb.[60]

$$\mathrm{TLE} = \sqrt[3]{\frac{\rho(T_0)}{\rho(T)}} - 1$$

where

$$\begin{aligned} \rho(\mathrm{Kg/m^3}) &= \rho_\alpha f_\alpha + \rho_\gamma f_\gamma + \rho_\delta f_\delta + \rho_l f_l \\ \rho_\alpha &= 7881 - 0.324T(^\circ\mathrm{C}) - 3 \times 10^{-5} T(^\circ\mathrm{C})^2 \\ \rho_\gamma &= \frac{100(8106 - 0.51T(^\circ\mathrm{C}))}{(100 - (\text{pct C}))(1 + 0.008(\text{pct C}))^3} \\ \rho_\delta &= \frac{100(8011 - 0.47T(^\circ\mathrm{C}))}{(100 - (\text{pct C}))(1 + 0.013(\text{pct C}))^3} \\ \rho_l &= 7100 - 73(\text{pct C}) - (0.8 - 0.09(\text{pct C})) \\ &\quad (T(^\circ\mathrm{C}) - 1550) \end{aligned} \quad [45]$$

A simple mixture rule is applied to obtain the overall density from the values of the different phases. Figure 10 shows the thermal linear-expansion curves for typical plain-carbon steels, assuming the arbitrary reference temperature, T_0, to be the solidus temperature.

D. *Inelastic Constitutive Properties*

The unified constitutive model developed here uses the instantaneous equivalent inelastic strain rate, $\dot{\bar{\varepsilon}}_{in}$, as the scalar-state function, which depends on the current equivalent stress, temperature, steel carbon content, and the current equivalent inelastic strain, which accumulates below the solidus temperature.[61,62,63] The model was developed to match tensile-test measurements of Wray[62] and creep-test data of Suzuki *et al.*[64]

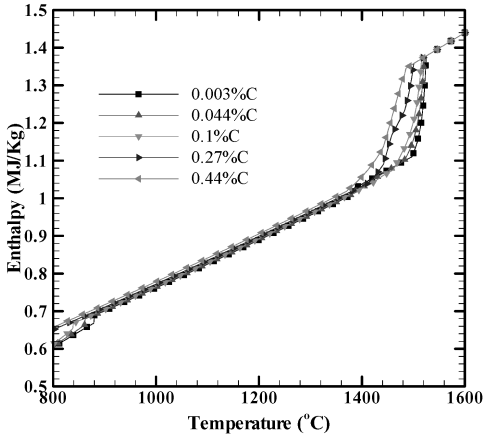

Fig. 9—Enthalpy of plain carbon steels.

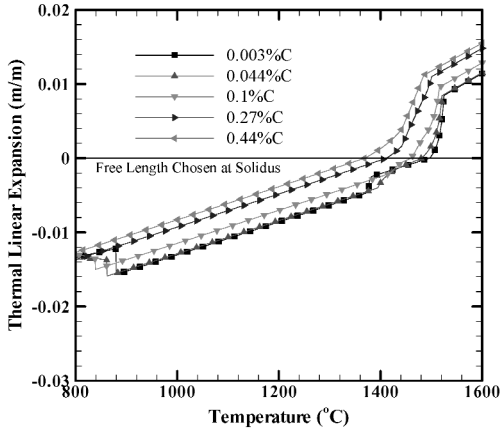

Fig. 10—Thermal linear expansion (TLE) of plain carbon steels.

Model III by Kozlowski, given in Eq. [46], is adopted to simulate the mechanical behavior of austenite.

$$\dot{\bar{\varepsilon}}_{in-\gamma}(1/s) = f_{pctC}|F_\gamma|^{f_3-1} F_\gamma \exp\left(-\frac{4.465 \times 10^4}{T(\mathrm{K})}\right)$$

where

$$\begin{aligned} F_\gamma &= c\bar{\sigma}\,(\mathrm{MPa}) - f_1\bar{\varepsilon}_{in}|\bar{\varepsilon}_{in}|^{f_2-1} \\ f_1 &= 130.5 - 5.128 \times 10^{-3} T(\mathrm{K}) \\ f_2 &= -0.6289 + 1.114 \times 10^{-3} T(\mathrm{K}) \\ f_3 &= 8.132 - 1.54 \times 10^{-3} T(\mathrm{K}) \\ f_{pctC} &= 4.655 \times 10^4 + 7.14 \times 10^4(\mathrm{pct\ C}) \\ &\quad + 1.2 \times 10^5(\mathrm{pct\ C})^2 \end{aligned} \qquad [46]$$

where the direction of $\bar{\sigma}$ (c) is given in Eq. [13], except using the principal stresses instead of principal strain components.

A power-law model was developed to model the behavior of δ-ferrite,[11] given as follows:

$$\dot{\bar{\varepsilon}}_{in-\delta}(1/s) = 0.1 F_\delta |F_\delta|^{n-1}$$

where

$$\begin{aligned} F_\delta &= \frac{c\bar{\sigma}(\mathrm{MPa})}{f_c(T(\mathrm{K})/300)^{-5.52}\left(1 + 1000|\bar{\varepsilon}_{in}|\right)^m} \\ f_C &= 1.3678 \times 10^4(\mathrm{pct\ C})^{-5.56\times10^{-2}} \\ m &= -9.4156 \times 10^{-5} T(\mathrm{K}) + 0.349501 \\ n &= (1.617 \times 10^{-4} T(\mathrm{K}) - 0.06166)^{-1} \end{aligned} \qquad [47]$$

Figure 11 compares the stresses measured by Wray[62] to those predicted by the constitutive models at 5 pct strain, integrated under different constant strain rates. The constitutive models give acceptable performance. This figure also shows that δ-ferrite, which forms at higher temperatures found near the solidification front, is much weaker than austenite. This greatly affects the mechanical behavior of the solidifying steel shell.

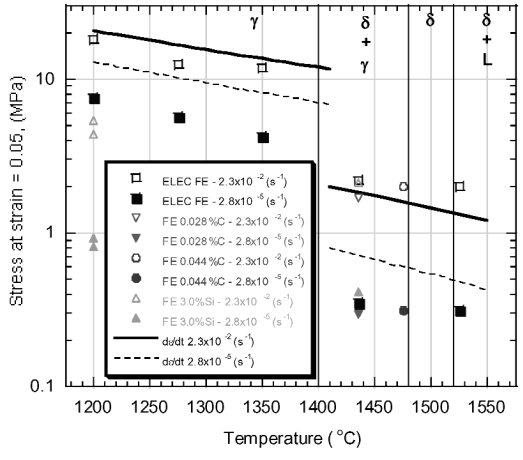

Fig. 11—Comparison of CON2D predicted and measured stress[62] at 5 pct plastic strain.

A simple mixture rule is not appropriate in two-phase regions that contain interconnecting regions of a much weaker phase. Thus, the constitutive model given in Eq. [47] is applied in the solid whenever the volume fraction of ferrite (δ-ferrite above 1400 °C, α-ferrite below 900 °C) is more than 10 pct. Otherwise, Eq. [46] is adopted.

To make the constitutive model properly handle kinematic hardening during reverse loading, the equivalent stress/strain used in Eqs. [46] and [47] is given the same sign as the principal stress/strain having the maximum magnitude. The inelastic strain rate, as a consequence, also bears a sign.

Two uniaxial tensile experiments[42,63] and a creep experiment[64] on plain-carbon steel at elevated temperatures were simulated by CON2D to test the performance of its constitutive models. Figures 12(a) and (b) show CON2D predictions of tensile-test behavior of austenite and delta-ferrite at constant strain rate around 10^{-4} s^{-1}, which is typically encountered in the shell during continuous casting.[63] The results also compare reasonably with experiments at small strain (<5 pct), although they overpredict the stress when the strain exceeds 5 pct. Because the strain generally stays within 5 pct for the entire continuous casting process, the constitutive models are quite reasonable for this purpose. Figure 13(a) shows the CON2D predictions of creep-test behavior at constant load. The inelastic-strain predictions match the measurements rea-

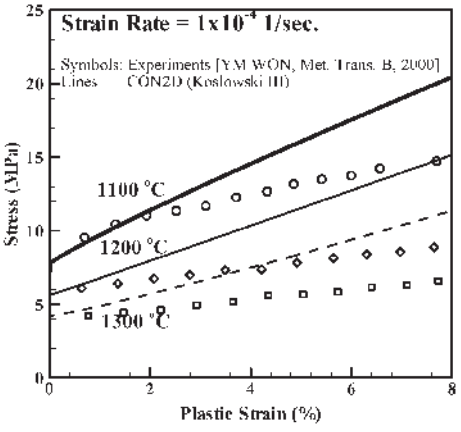

(*a*)

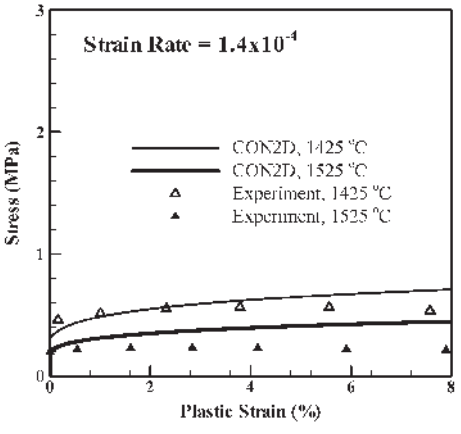

(*b*)

Fig. 12—CON2D predictions compared with tensile-test measurements:[42,62] (*a*) Koslowski III law for austenite[61] against tensile test measurements[62] and (*b*) Power law for δ-ferrite[3] against tensile test measurements.[62]

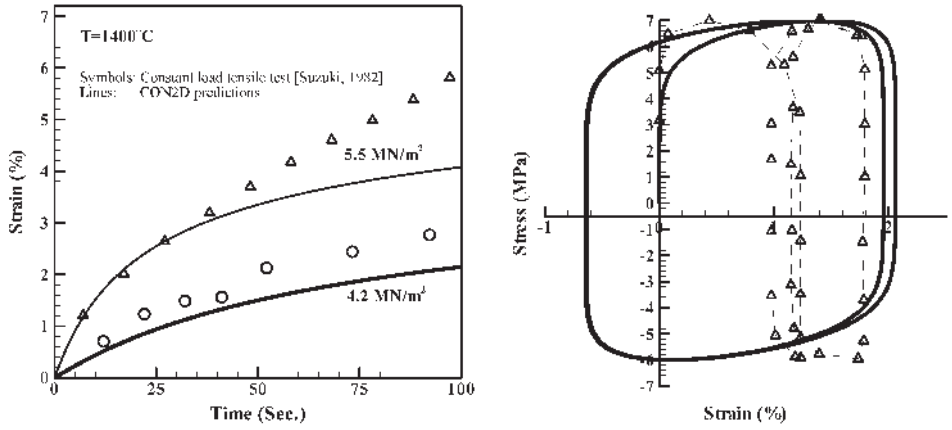

(*a*) (*b*)

Fig. 13—Predicted behavior of austenite compared with creep and cyclic loading test measurements at 1300 °C:[64] (*a*) constant load and (*b*) alternating load.

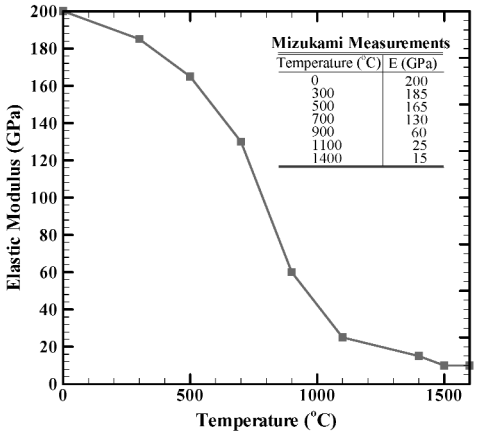

Fig. 14—Elastic modulus for plain carbon steels used in CON2D.[65]

sonably well, especially at times shorter than 50 seconds, of most concern to continuous casting in the mold region. Beyond this time, CON2D underpredicts creep, which is consistent with the overprediction of stress, observed in the tensile test cases. Monotonic loading is unlikely beyond this length of time, anyway. Figure 13(b) compares CON2D predictions and creep-test measurements[64] under a sinusoidal alternating load with full reversal (R ratio = 1.167). Although more measurements and computations of complex loading conditions would be helpful, these comparisons show that the constitutive models in CON2D are reasonable, even for conditions that include reverse loading.

E. *Elastic Properties*

The temperature-dependent elastic-modulus curve used in this model is a stepwise linear fit of measurements by Mizukami *et al.*,[65] given in Figure 14. Unlike in some other models, the elastic modulus of the liquid here was given the physically realistic value of 10 GPa. The Poisson ratio ν is constant at 0.3. Measurements of higher Poisson ratios at high temperature are attributed to creep occurring during the experiment. Incorrectly incorporating part of the volume-conserved plastic behavior, where $\nu = 0.5$, into the elastic ν would cause numerical difficulty for the solver.

XI. NUMERICAL PERFORMANCE

A 2-D transient elastic-viscoplastic thermal-stress simulation with solidification, internal pressure, and contact is a challenging problem even for a supercomputer. The efficient algorithms in CON2D allow the complete solution of practical problems in reasonable times with reasonable accuracy. Coupling between the thermal and stress models can cause instability, however, unless parameters such as time-step size, tolerances of gap size, and penetration are carefully chosen. Current experience indicates that the initial time step for a fully coupled simulation with mold wall constraint should be 0.0001 seconds, which is 10 times smaller than the smallest time step size adopted for the uncoupled thermal-stress simulation by Zhu.[3] The time-step size can be increased twentyfold up to 0.005 seconds as the simulation progresses. Increasing the time-step size further does not speed up the simulation due to the need for more in-step iterations. It takes about 72 hours to perform a complete, fully coupled 19-second mold simulation of a 120 × 120 mm billet with 7381 nodes on a PENTIUM* IV 1.7 GHz workstation running the WINDOWS* 2000 Professional operating system using less than 500 MB of random-access memory. The corresponding simulation without coupling allows larger time steps (0.001 to 0.5 seconds) and takes only about 5 hours. Below-mold simulations allow even larger steps and take only about 1 hour.[66]

*PENTIUM is a trademark of the Intel Corporation, Santa Clara, CA.

*WINDOWS is a trademark of the Microsoft Corporation, Redmond, CA.

Reasonable tolerances should be specified to achieve satisfactory gap-size convergence while avoiding excessive mold wall penetration. The minimum gap, d_{gapmin}, is chosen here to be 0.012 mm, which is less than the effective thickness of the oscillation marks and surface roughness. Gaps smaller than this are considered to be converged. Thus, the effective oscillation mark-depth dominates the heat resistance across the gap and must be determined either by measurement or calibration. The tolerance for the mold wall penetration, d_{pen}, is chosen to be 0.001 mm, which is on the order of the incremental displacement between two consecutive time steps. Too large a tolerance tends

to make the simulation inaccurate, while too small a tolerance makes the program overreact to small penetrations and slows down the simulation. The best value of d_{pen} depends on the problem. Generally, a smaller value is needed when the simulation region of interest is closer to the meniscus.

XII. MODEL VALIDATION

An analytical solution of the thermal-stress model in an unconstrained solidifying plate, derived by Weiner and Boley,[67] is used here as an ideal validation problem for solidification-stress models. Constants for this validation problem were chosen here to approximate the conditions of interest in this work and are listed in Table II.

The material in this problem has elastic–perfect plastic behavior. The yield stress drops linearly with temperature from 20 MPa at 1000 °C to 0 MPa at the solidus temperature of 1494.35 °C. For the current elastic-viscoplastic model, this constitutive relation was transformed into a computationally more challenging form, the highly nonlinear creep function of Eq. [14] with $A = 1.5 \times 10^8$ and $\sigma_{yield} = 0.01$ MPa in the liquid. A very narrow mushy region, 0.1 °C, is used to approximate the single melting temperature assumed by Boley and Weiner. In addition to the generalized plane-strain condition in the axial z direction, a similar condition was imposed in the y direction (parallel to the surface) by coupling the displacements of all nodes along the top surface of the slice domain, as shown in Figure 1(c). The analytical solutions were computed with MATLAB.[68]

Figures 15 and 16 show the temperature and the stress distributions across the solidifying shell at different solidification times using an optimized mesh and time step, similar to that adopted for the 2-D billet-casting simulation. The mesh was graduated, increasing in size from 0.3 mm at the left-hand end to 2.0 mm at right-hand end, and the time-step size increased from 0.001 seconds at the beginning to 0.1 seconds at the end.

Figures 17 and 18 show the relative average errors, given in Eq. [48] for the temperature and stress predictions, respectively.

$$\text{Error}_T\,(\text{pct}) = \frac{\sum_1^N \sqrt{\left(T_i^{\text{CON2D}} - T_i^{\text{Analytical}}\right)^2}}{N\,|T_{\text{melt}} - T_{\text{cold}}|} \times 100$$

$$\text{Error}_\sigma\,(\text{pct}) = \frac{\sum_1^N \sqrt{\left(\sigma_i^{\text{CON2D}} - \sigma_i^{\text{Analytical}}\right)^2}}{N\,|\sigma\,(T_{\text{melt}}) - \sigma\,(T_{\text{cold}})|} \times 100 \qquad [48]$$

Accuracy of the CON2D predictions increases if the mesh and time step are refined together. A fine uniform mesh of 0.1 mm, with a small uniform time step of 0.001 seconds, produces relative average errors within 1 pct for temperature and within 2 pct for stress. However, the computational cost is also high. Note that the inaccuracy is severe at early times of the simulation, especially for the stress predictions. This is because the solidified layer initially spans only a few elements. As the solid portion of the plate grows thicker, the mesh size and time-step requirements become less critical. Thus, a nonuniform mesh with increasing time-step size is better to satisfy both accuracy and efficiency. The optimal choice, used in Figures 15 and 16, gives a decent prediction with the relative average errors within 2 pct for temperature and 3 pct for stress. A similar mesh was adopted for the actual billet-casting simulation. This demonstrates that the model is numerically consistent and has an acceptable mesh.

Table II. Constants Used in Boley and Weiner Analytical Solution

Conductivity (W/m K)	33.0
Specific heat (kJ/kg K)	0.661
Latent heat (kJ/kg)	272.0
Elastic modulus in solid (GPa)	40.0
Elastic modulus in liquid (GPa)	14.0
Thermal linear expansion coefficient (1/K)	0.00002
Density (kg/m^3)	7500.0
Poisson's ratio	0.3
Melting temperature, T_{melt} (°C)	1494.4
Liquidus temperature (°C)	1494.45
Solidus temperature (°C)	1494.35
Cold surface temperature, T_{cold} (°C)	1000.0

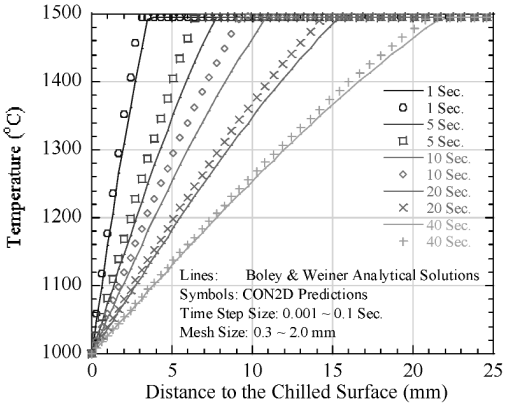

Fig. 15—Temperatures through an infinite solidifying plate at different solidification times compared with Boley & Weiner analytical solution.

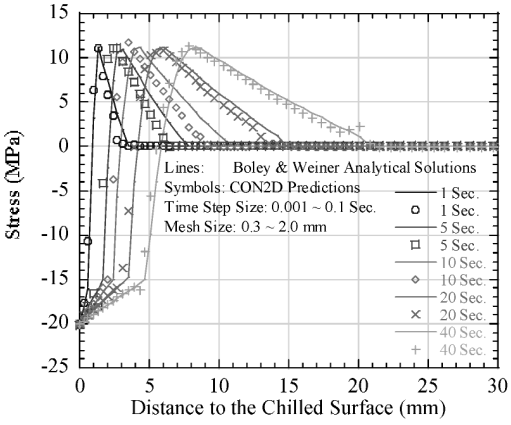

Fig. 16—Stresses through an infinite solidifying plate at different solidification times compared with Boley & Weiner analytical solution.

XIII. APPLICATION TO BILLET CASTING

The CON2D model was next applied to simulate a plant trial conducted at POSCO (Pohang works, South Korea[18]) for a 120-mm-square section billet of 0.04 pct C steel cast at 2.2 m/min, where measurements were available. The mold

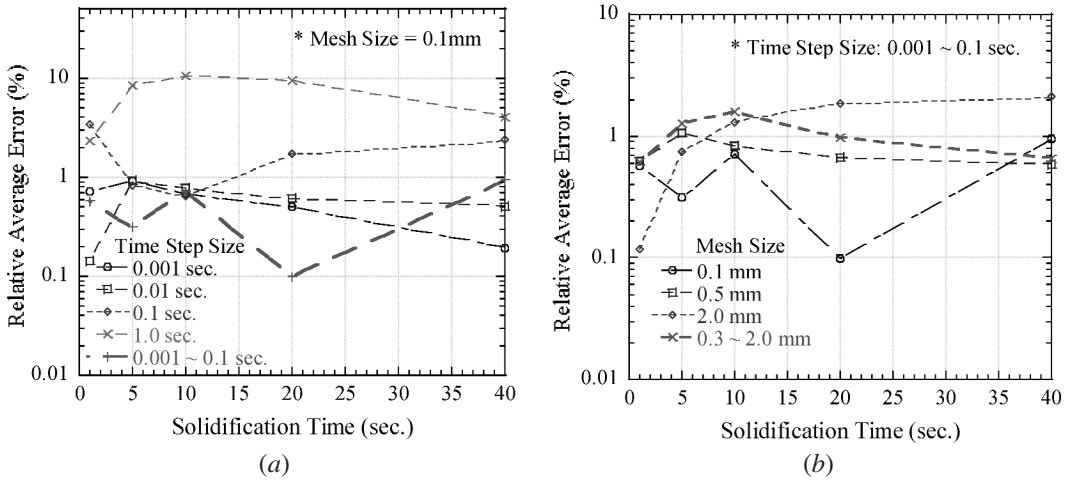

Fig. 17—Temperature error between CON2D and analytical solution[67] from convergence studies: (*a*) time-step size effect and (*b*) mesh size effect.

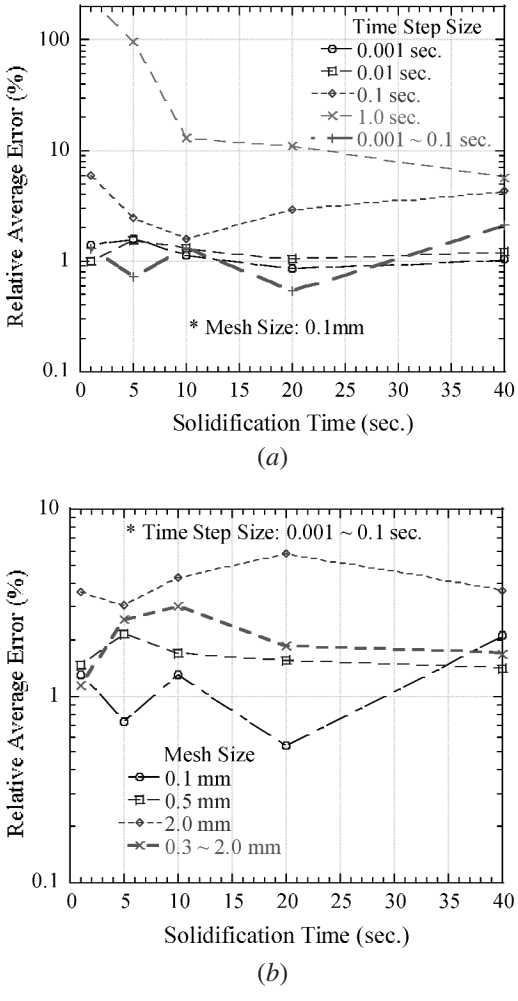

Fig. 18—Stress error between CON2D and analytical solution[67] from convergence studies: (*a*) time-step size effect and (*b*) mesh size effect.

had a single linear taper of 0.785 pct/m. Details of the material and operation conditions are given in Tables III and IV, respectively. Two simulations were performed to predict the temperature, stress, and deformation evolutions of the billet

Table III. Material Details in Billet Plant Trial

Steel composition (wt pct)	0.04C
Liquidus temperature (°C)	1532.1
70 pct solid temperature (°C)	1525.2
90 pct solid temperature (°C)	1518.9
Solidus temperature (°C)	1510.9
Austenite → α-ferrite starting temperature (°C)	781.36
Eutectoid temperature (°C)	711.22

Table IV. Simulation Conditions in Billet Plant Trial

Billet section size (mm × mm)	120 × 120
Working mold length (mm)	700
Total mold length (mm)	800
Casting speed (m/min)	2.2
Mold corner radius, (mm)	4
Taper (pct m)	0.785 (on each face)
Time to turn on ferrostatic pressure (s)	2.5
Mesh size (mm × mm)	0.1 × 0.1 to 1.4 × 1.0
Number of nodes (varies with section size)	7381
Number of elements (varies with section size)	7200
Time step size (s)	0.0001 to 0.005
Pouring temperature (°C)	1555.0
Coherency temperature (°C)	1510.9
Gap tolerance, d_{min}	0.001 (0.1 pct)
Minimum gap, d_{gapmin} (mm)	0.012
Penetration tolerance, d_{pen} (mm)	0.001

shell using the 2-D L-shaped domain (Figure 1(b)) and a slice domain through the centerline of the billet face (Figure 1(c)), similar to the Boley and Weiner analytical problem. The interfacial heat-transfer constants for both simulations are given in Table I and were found with the help of a dedicated heat-transfer code, CON1D.[51]

The superheat-flux profile was obtained from coupled computations of turbulent flow and heat transfer in a round billet caster by Khodadadi *et al.*[54] for the case of a Grashof number ($Gr = gW^3$ (TLE(T_{pour}) − TLE(T_m))/ν^2) of 1×10^8. This value is the closest case to the current problem conditions,

where the Grashof number is 2×10^7, and confirms that natural convection is unimportant in this process. The heat flux was calculated from the Nusselt number (Nu) and mean liquid temperature (T_m) results, given as a function of distance below the meniscus,[54] using their values of liquid steel conductivity, $k = 29.8$ W/mK, mold section size, $W = 200$ mm, and 33 °C superheat, except for readjusting the superheat temperature difference as follows:

$$q_{sup} = \frac{\mathrm{Nu}\, k(T_m - T_{liq})}{W} \frac{(T_{pour} - T_{liq})_{Posco}}{(T_{pour} - T_{liq})_{Khodadadi}} \quad [49]$$

where T_{pour} and T_{liq} are the pouring and liquidus temperatures, respectively. The resulting superheat-flux profile is shown in Figure 19. Note that the total heat integrated from Figure 19 over the mold surface, 48.6 kW, matches the superheat for the current problem, $(T_{pour} - T_{liq})\rho c_p \nu_c = 46$ kW.

The heat-flux and mold wall temperatures predicted by CON2D along the billet-face center are shown in Figures 20 and 21, respectively. These results slightly underpredict the measurements of thermocouples embedded in the mold wall, which should lie almost exactly between the hot- and cold-face temperatures.[69] The total heat extracted by the mold (128.5 kW) is 17 pct lower than the plant measurements, based on a heat balance of the mold cooling water (8 K temperature rise at a 9.2 m/s slot velocity) of 154 kW.[18] This is consistent with underprediction of the mold temperatures.

The predicted shell growth for this CON2D simulation is given in Figure 22, as indicated by the evolution of the solidus and liquidus isotherms. This is compared with measurements of the solid/liquid interface location, obtained by suddenly adding FeS tracer into the liquid pool during steady-state casting.[18] Longitudinal and transverse sections through the billet were cut from the final product. The transverse section was 285 mm from the meniscus when the FeS tracer was added. Because FeS tracer cannot penetrate the solid steel shell, sulfur prints of sections cut through the fully solidified billet reveal the location of the solidification front and shell-thickness profile at a typical instant during the process.[18] The CON2D predictions match along the centerline beyond the first 80 mm below the meniscus, where the shell remains in contact with the mold, suggesting that the heat-transfer parameters are reasonably accurate.

The shell-surface-position profile down the centerline is shown in Figure 23, together with the mold wall position, which includes both the taper and the mold-distortion profile calcu-

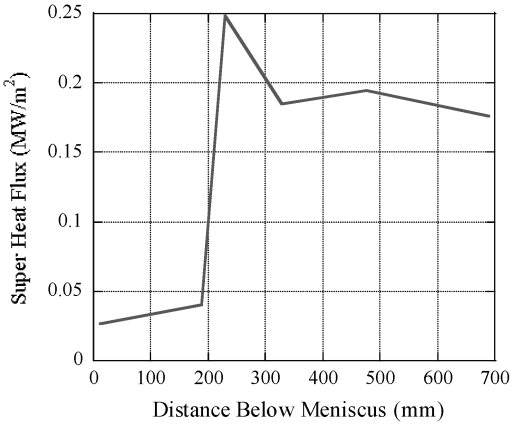

Fig. 19—Super heat flux used in CON2D for billet casting simulation.

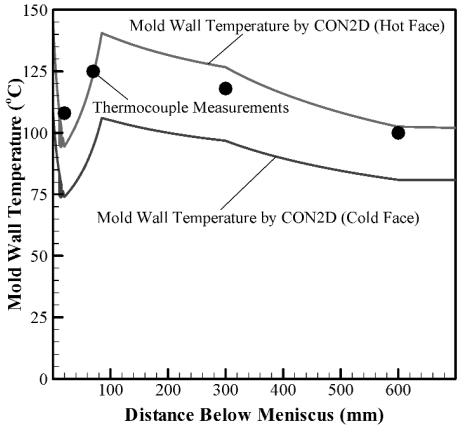

Fig. 21—Predicted mold wall temperature profiles compared with plant measurements.

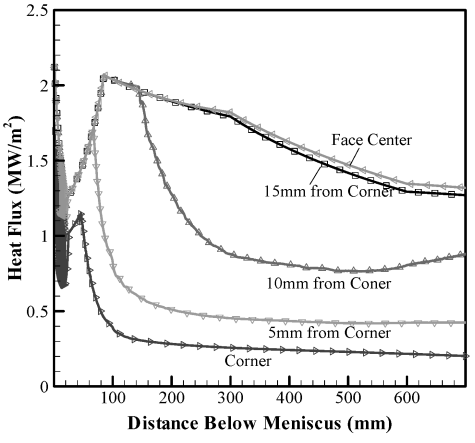

Fig. 20—Predicted instantaneous heat flux profiles in billet casting mold.

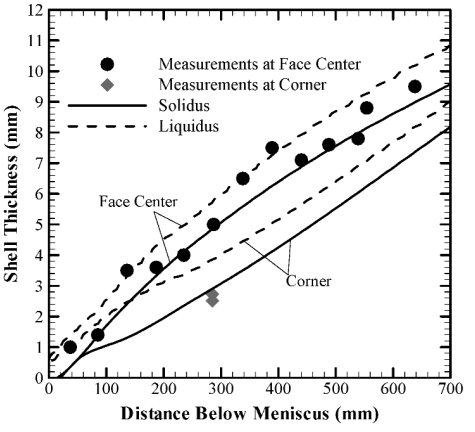

Fig. 22—Predicted shell thickness profiles for billet casting compared with plant measurements.

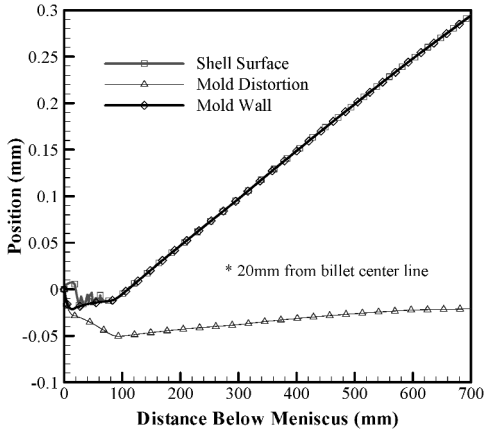

Fig. 23—Mold distortion, mold wall position, and shell surface profiles for the billet casting simulation.

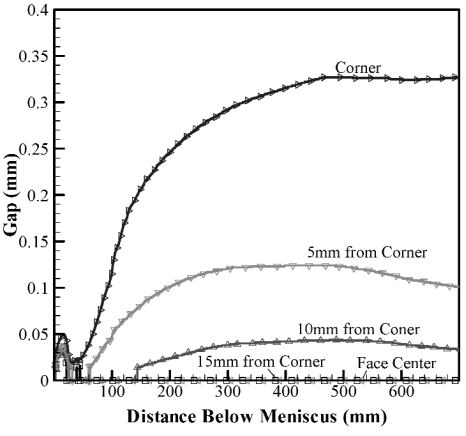

Fig. 24—Gap evolution predicted by CON2D for the billet casting simulation.

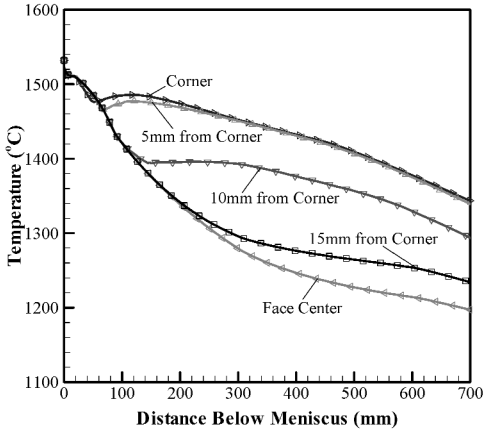

Fig. 25—Shell surface temperatures predicted for billet casting simulation.

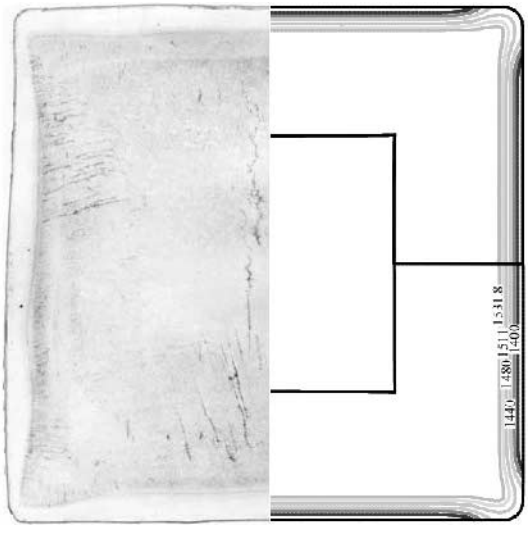

Fig. 26—Temperature contours at 285 mm below meniscus compared with corresponding sulfur print from plant trial.

lated from the CON1D temperature results using Eq. [39].[51] The shell surface generally follows the mold wall with no obvious penetration, validating the contact algorithm. Note, however, that a slight gap opens up within the first 25 mm. Although this effect is believed to be physically reasonable owing to rapid initial shrinkage of the steel, it is exaggerated here, owing to numerical difficulties during the initial stages of solidification. This causes an overprediction of the drop in initial heat flux and temperature observed in Figure 20. This drop is followed by increased heat flux (and corresponding mold wall temperature) after full contact is re-established, which has also been observed in other measurements.[70]

The simulation features a detailed prediction of temperature, shrinkage, and stress in the region of the rounded billet corner. The evolution of the increases in gap size and surface temperature are given in Figures 24 and 25 near (20 mm) to the centerline of the billet face and at various locations 0, 5, 10, and 15 mm from the billet corner. The corresponding large drops in heat flux are included in Figure 20. The solidifying shell quickly becomes strong enough to pull the billet corner away from the mold wall and form a gap around the corner region. The gap greatly decreases local heat flow in the corner, causing the mold wall temperature to drop.

The drop in mold temperature near the corner over the initial 80 mm is more than expected in reality, because the simple mold model of CON2D in Eq. [33] neglects heat conduction around the corner and along the casting direction. Thus, these predictions are not presented. This latter effect, which is included in CON1D,[51] also contributed to the convergence difficulties along the centerline discussed in Figure 23. Fortunately, it has little other effect on heat flux or shell behavior.

Figure 24 shows how a permanent gap forms after 40 mm below the meniscus, which grows to over 0.3-mm thick by halfway down the mold, growing little after that. Corresponding gaps form adjacent to the corner at later times, reaching smaller maxima partway down the mold. These gaps form because the simple linear taper of the mold walls was insufficient to match shrinkage of the shell. The corner effect decreases with distance from the corner and disappears beyond 15 mm from the corner.

The corner gap and drop in heat flux cause a hot spot at the corner region, as shown in the surface-temperature profiles of Figure 25. The CON2D model predicts that the shell corner reheats slightly and becomes 150 °C hotter than billet-face center, for the conditions of this trial. The decreased heat flux also produces less solidification in the corner, as illustrated in Figure 26 at 285 mm below the meniscus. The predicted shell

thinning around the corner is consistent with the plant measurements from the sulfur print, as quantified in Figures 22 and 26. The predictions here are also consistent with those of Park *et al*., who modeled how increasing the billet-mold corner radius leads to more severe hot and thin spots near the corner.[18] This tends to validate the CON2D model and the simple constant interfacial heat-transfer parameters used to produce these results. Improving the accuracy would likely require a more complex model of gap heat transfer that considered details of surface roughness, including differences between the center and corner.

Figure 27 shows the evolution of surface-stress components near the centerline of the billet face. Stress normal to the surface (*x* direction) is effectively equal to zero, which indicates that the 0.785 pct/m mold taper never squeezes the billet. The stress components perpendicular to the solidification direction (*y* direction tangential to the surface and *z* casting direction) are generally very similar, which matches the behavior expected from the analytical test solution.[67] These stresses grow slowly in tension during the period of increasing heat-extraction rate from 20 to 100 mm below the meniscus. They reach a maximum of almost 3 MPa due to the increase in shell strength at lower temperature that accompanies the transformation from δ-ferrite to austenite. This is shown in the through-thickness profile of these same stress components in Figure 28(a), but is calculated with the 1-D slice domain. The surface tensile-stress peak does not penetrate very deep, owing to the very thin layer of material colder than 10 pct delta-ferrite. Thus, this peak might cause very shallow fine surface cracks, but nothing deeper.

The surface stresses in Figure 27 suddenly turn compressive beyond 100 mm due to the sudden change in heat-extraction rate at this distance (Figure 20). Surface compression arises because the subsurface begins to cool and shrink faster than the surface. This causes a corresponding increase in subsurface tension near the solidification front that might lead to subsurface cracks. The surface stays in compression from -4 to -6 MPa for the remaining time in the mold.

During the time beyond 100 mm, the stress profile (Figure 28(b)) is qualitatively similar to that of the analytical test problem, as expected. Differences arise from the variation in steel strength between the δ-ferrite and austenite. Stresses in the liquid, mushy zone, and δ-ferrite are always very small. Tensile stress increases rapidly during the phase transformation, which takes place at the low end of the $\delta + \gamma$ region of Figure 28. When the δ-ferrite region is thin, this tensile stress is more likely to create strains significant to generate cracks. These results illustrate the widely accepted knowledge that surface cracks initiate near the meniscus, while subsurface cracks form lower down.

Figures 29(a) and (b) show the different components of strain (*y* direction) through the shell thickness near the billet-face center corresponding to the stresses in Figure 28. Thermal strains dominate in the solid and generate the other strains due to the constraint of adjacent layers of steel. Small elastic strains are generated by the mismatch of thermal strain, although the stresses they generate may still be significant. Inelastic strain is generated in regions of high stress, starting in the $\delta + \gamma$ region. It is high at the surface at the top of the mold and later grows in the austenite. Note that inelastic strains are all tensile throughout the shell. The δ and mushy zones behave elastically with very low stresses. This is fortunate, as these phases are very weak and cannot accommodate much inelastic strain before cracking. Flow strain in the liquid occurs to accommodate the total strain, which is naturally flat, owing to the constraint by the solid.

Figure 30 shows the "hoop" stress component (*y* direction parallel to the billet surface and perpendicular to the

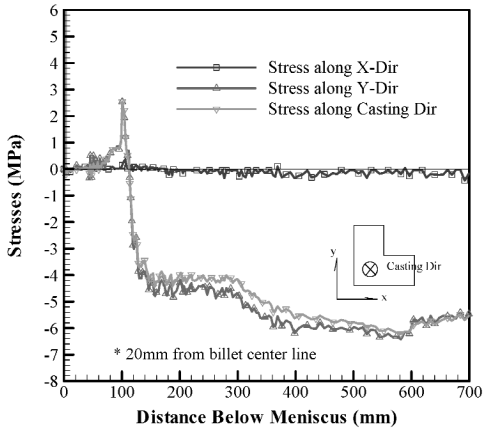

Fig. 27—Surface stress histories predicted near the billet face center (2-D L-mesh domain).

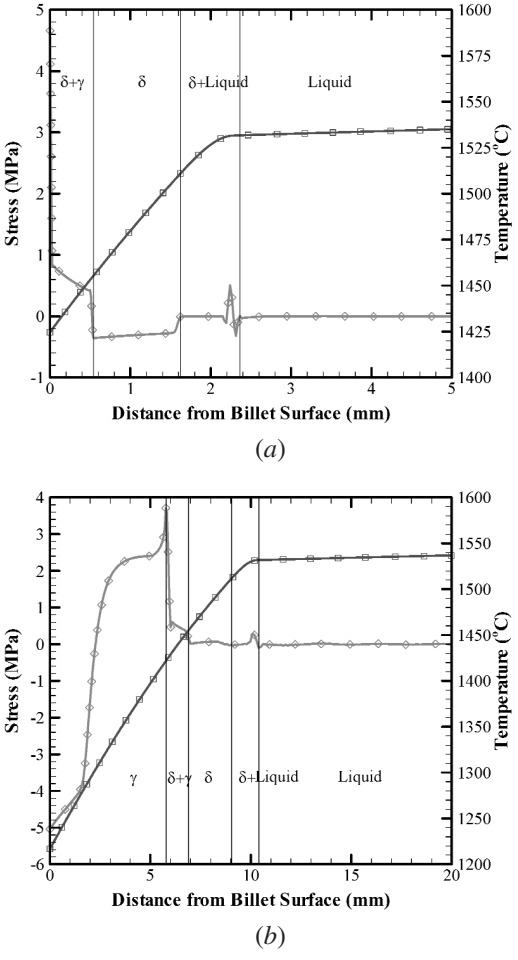

Fig. 28—Stress and temperature predicted through the shell thickness far from billet corner (slice domain): (*a*) 100 mm below meniscus and (*b*) mold exit (700 mm below meniscus.

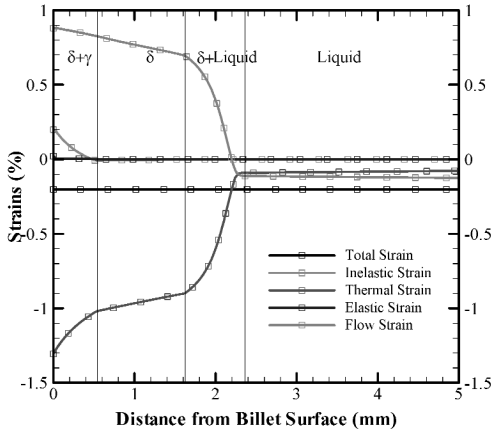

(*a*)

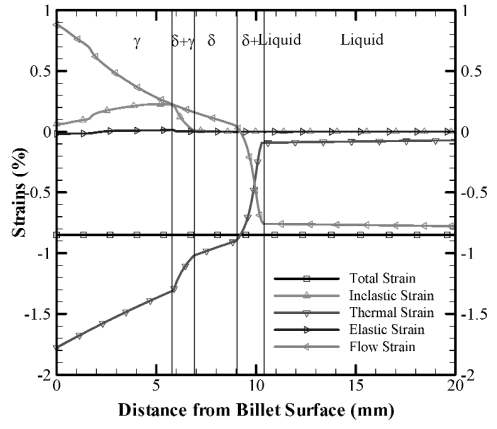

(*b*)

Fig. 29—Strain components predicted through the shell thickness far away from billet corner (slice domain): (*a*) 100 mm below meniscus and (*b*) mold exit (700 mm below meniscus).

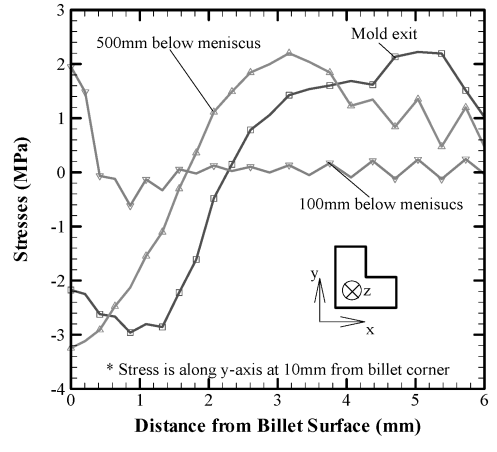

Fig. 30—Stress predicted through the shell thickness near billet corner (2-D L-mesh domain).

casting direction) at an off-corner location (10 mm above the billet corner) through the shell thickness at 100, 500, and 700 mm (mold exit) below the meniscus. Stresses all behave similarly to the corresponding locations along the billet centerline, except that the tension and compression are lower. This is expected due to the slower cooling rates, shallower temperature gradients, and higher temperatures near the corner.

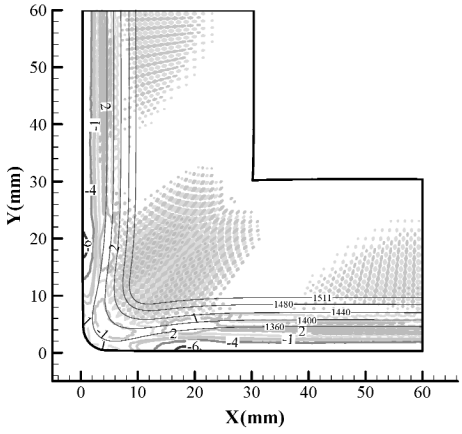

Fig. 31—Stress contours predicted at mold exit.

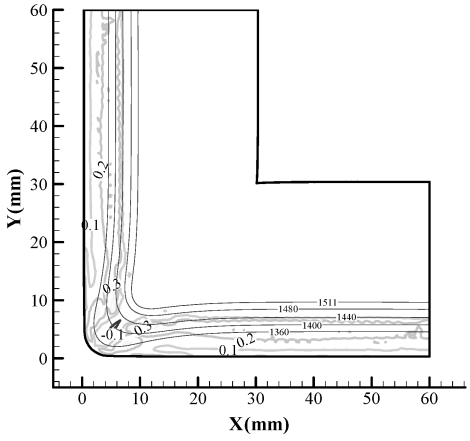

Fig. 32—Inelastic strain contours predicted at mold exit.

Figures 31 and 32 show contours of the stress and inelastic strain components perpendicular to the solidification direction superimposed on the distorted billet at the mold exit with isotherms. The insufficient 0.785 pct/m taper of this mold is unable to support the billet, which allows a slight bulge (0.25 mm at the mold exit). Regions of high tensile stress and inelastic strain are indicated at the off-corner subsurface (10 to 20 mm from the corner and 2 to 6 mm beneath the surface).

XIV. CONCLUSIONS

A transient, two-dimensional, finite-element model has been developed to quantify the temperature, stress, and strain distributions in the solidifying shell in the continuous casting of steel. This is a Lagrangian approach in generalized plane strain that reasonably predicts the 3-D stress and strain state by solving energy- and force-balance equations within a 2-D transverse slice domain. Superheat dissipation and ferrostatic pressure are both taken account of through internal boundary conditions. Unified elastic-viscoplastic constitutive models for both the austenite and δ-ferrite phases of the steel match tensile- and creep-test data. Liquid is given physically reasonable properties, including a high viscoplastic shear rate and small yield

stress. A robust and efficient time-integration technique, the alternating local-global method, is adopted to integrate the highly nonlinear constitutive equations. An efficient contact algorithm allows the model to properly treat shell-surface interaction with the mold wall.

The model is validated by extensive comparisons with an analytical solution of thermal stress in an infinite solidifying plate, which justify the choice of mesh and time-step size. The model is applied to simulate a 120-mm-square billet continuously cast at 2.2 m/min, and the results compare favorably to in-plant measurements of thermocouples embedded in the mold walls, heat balance on the cooling water, and thickness of the solidified shell.

The CON2D model is a useful tool to gain quantitative understanding of issues pertaining to the thermal-mechanical behavior of the solidifying shell during the continuous casting of steel slabs and billets. It is being applied to investigate taper in billets[71] and slabs,[72] minimum shell thickness to avoid breakouts,[30] maximum casting speed to avoid longitudinal cracks due to off-corner bulging below the mold,[66] and other phenomena.[75]

ACKNOWLEDGMENTS

The authors thank the steel industry members of the Continuous Casting Consortium at UIUC for their financial support of this project. Work by previous students, A. Moitra, H. Zhu, and J. Parkman, on the CON2D program is also gratefully acknowledged. The authors also thank the National Center for Supercomputing Applications (NCSA) for computational resources.

APPENDIX A

Finite-element implementation of heat-transfer model

A. *Linear Temperature Triangles*

The small triangles in Figure [A1] show the constant temperature-gradient triangle element used for the heat-flow model. Temperature within an element is interpolated by the same shape functions used to interpolate the coordinates.

$$T = \sum_{i=1}^{3} N_i(x, y) T_i \qquad [A1]$$

The $[B]$ matrix in global coordinate system can be obtained as

$$[B] = \frac{1}{2A}\begin{bmatrix} y_2 - y_3 & y_3 - y_1 & y_1 - y_2 \\ x_3 - x_2 & x_1 - x_3 & x_2 - x_1 \end{bmatrix} \qquad [A2]$$

where A is the area of the triangle element.

B. *Conductance Matrix and Capacitance Matrix*

The element conductance and capacitance matrices needed to assemble Eq. [15] are given in Eqs. [A3] and [A4].[73]

$$[K]_{el} = \int [B]^T \begin{bmatrix} k_e & 0 \\ 0 & k_e \end{bmatrix} [B] dA \qquad [A3]$$

$$[C]_{el} = \int [N]^T \rho c_{pe} [N] dA = \frac{\rho c_{pe} A}{12}\begin{bmatrix} 2 & 1 & 1 \\ 1 & 2 & 1 \\ 1 & 1 & 2 \end{bmatrix} \qquad [A4]$$

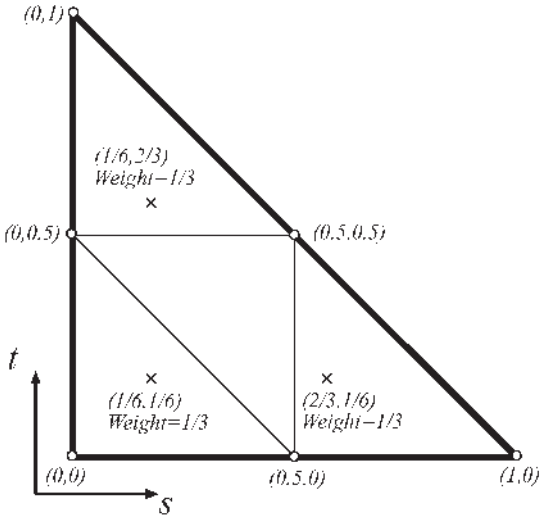

Fig. A1—Six-node quadratic displacement triangle element with Gauss points for stress model and corresponding 4 three-node linear temperature triangle elements.

where k_e is the average conductivity of the three nodal values within each element and c_{pe} is the effective specific heat within the element, given by Eq. [16].

APPENDIX B

Finite-element implementation of stress model

A. *Linear Strain Elements*

Figure [A1] shows the six-node linear-strain isoparametric triangle finite element used in this work. Global coordinates and displacements within each element are interpolated from its nodal values by

$$\begin{Bmatrix} x \\ y \end{Bmatrix} = \sum_{i=1}^{6} \begin{bmatrix} N_i & 0 \\ 0 & N_i \end{bmatrix} \begin{Bmatrix} x_i \\ y_i \end{Bmatrix} \qquad [B1]$$

$$\begin{Bmatrix} u \\ v \end{Bmatrix} = \sum_{i=1}^{6} \begin{bmatrix} N_i & 0 \\ 0 & N_i \end{bmatrix} \begin{Bmatrix} u_i \\ v_i \end{Bmatrix} \qquad [B2]$$

where the shape functions in natural local coordinates are

$$[N_{i=1,2,\ldots,6}] = [s(2s-1)\; t(2t-1)\; r(2r-1)\quad 4st\quad 4tr\quad 4sr]$$
$$r = 1 - s - t \qquad [B3]$$

B. *Generalized Plane Strain Formulation*

The three unknowns, a, b, and c, which describe the out-of-plane strain in Eq. [5], are assembled into the finite-element equations to be solved concurrently within the in-plane displacements. The displacement vector is therefore

$$\begin{Bmatrix} \delta \\ 15\times 1 \end{Bmatrix} = \left\{ \begin{Bmatrix} u \\ 12\times 1 \end{Bmatrix}^T \quad a \quad b \quad c \right\}^T \qquad [B4]$$

where

$$\begin{Bmatrix} u \\ 12\times 1 \end{Bmatrix} = \left\{ u_1 \; \ldots \; u_6 \quad v_1 \; \ldots \; v_6 \right\}^T$$

The strain-displacement relationship is

$$\left\{\Delta\varepsilon_x \quad \Delta\varepsilon_y \quad \Delta\varepsilon_{xy} \quad \Delta\varepsilon_z\right\}^T = \left[\underset{4\times15}{B'}\right]\left\{\delta\right\} \qquad [B5]$$

The $[B']$ for matrix generalized plane strain is given as

$$\left[\underset{4\times15}{B'}\right] = \begin{bmatrix} \left[\underset{3\times12}{B}\right] & \left[\underset{3\times3}{0}\right] \\ \left[\underset{1\times12}{0}\right] & \begin{matrix} 1 & x & y \end{matrix} \end{bmatrix} \qquad [B6]$$

where

$$\left[\underset{3\times12}{B}\right] = \begin{bmatrix} \frac{\partial N_1}{\partial x} & \cdots & \frac{\partial N_6}{\partial x} & 0 & \cdots & 0 \\ 0 & \cdots & 0 & \frac{\partial N_1}{\partial y} & \cdots & \frac{\partial N_6}{\partial y} \\ \frac{\partial N_1}{\partial y} & \cdots & \frac{\partial N_6}{\partial y} & \frac{\partial N_1}{\partial x} & \cdots & \frac{\partial N_6}{\partial x} \end{bmatrix}$$

The elastic stress-strain relation is

$$\begin{Bmatrix} \Delta\sigma_x \\ \Delta\sigma_y \\ \Delta\sigma_{xy} \\ \Delta\sigma_z \end{Bmatrix} = [D]\left(\begin{Bmatrix} \Delta\varepsilon_x \\ \Delta\varepsilon_y \\ \Delta\varepsilon_{xy} \\ \Delta\varepsilon_z \end{Bmatrix} - \begin{Bmatrix} \Delta\varepsilon_T \\ \Delta\varepsilon_T \\ 0 \\ \Delta\varepsilon_T \end{Bmatrix} - \begin{Bmatrix} \Delta\varepsilon_{plx} \\ \Delta\varepsilon_{ply} \\ \Delta\varepsilon_{plxy} \\ \Delta\varepsilon_{plz} \end{Bmatrix} \right) \qquad [B7]$$

The deviatoric stress vector is

$$\left\{\sigma\right\}' = \left\{\sigma_x - \frac{1}{3}\sigma_m \quad \sigma_y - \frac{1}{3}\sigma_m \quad \sigma_z - \frac{1}{3}\sigma_m \quad \tau_{xy}\right\} \qquad [B8]$$

where

$$\sigma_m = \sigma_x + \sigma_y + \sigma_z$$

The von-Mises or "equivalent" stress is

$$\overline{\sigma} = \sqrt{\frac{1}{2}\left((\sigma_x - \sigma_y)^2 + (\sigma_x - \sigma_z)^2 + (\sigma_z - \sigma_y)^2 + 2\tau_{xy}^2\right)} \qquad [B9]$$

C. *Global Stiffness Matrix and Force Vectors*

The global stiffness matrix $[K]$, and force vectors, $\{\Delta F_{\varepsilon_{th}}\}$, $\{\Delta F_{\varepsilon_{pl}}\}$, $\{F_{fp}\}$, and $\{F_{el}\}$, in Eq. [21] are assembled from the local stiffness matrix and force vectors of each element at the current time step $t + \Delta t$.

$$[K] = \sum_{e=1}^{n} \int_{A_e} \left([B]_e\right)^T [D][B]_e \, dA \qquad [B10]$$

$$\{F_{fp}\} = \sum_{e=1}^{nb} \int_{L_{fp}} \left([N]_e\right)^T (F_p) dL_{fp} \qquad [B11]$$

$$\{\Delta F_{th}\} = \sum_{e=1}^{n} \int_{A_e} \left([B]_e\right)^T [D]\{\Delta\varepsilon^{th}\} dA \qquad [B12]$$

$$\{\Delta F_{in}\} = \sum_{e=1}^{n} \int_{A_e} \left([B]_e\right)^T [D]\{\Delta\varepsilon^{in}\} dA \qquad [B13]$$

$$\{F_{el}\} = \sum_{e=1}^{n} \int_{A_e} \left([B]_e\right)^T [D]\{\varepsilon^{el}\} dA \qquad [B14]$$

Integrals are evaluated numerically using standard second-order Gauss quadrature[74] according to the integration sampling points given in Figure 33 with a constant weighting factor of 1/3.

NOMENCLATURE

c_p	specific heat of steel (kJ/kg K)
c	sign of the equivalent stress/strain
E	Young's modulus (MPa)
F_p	ferrostatic pressure
g	gravity acceleration
H	enthalpy of steel (kJ/kg)
k	conductivity of steel (W/m K)
Nu	Nusselt number
q	heat flux
T	temperature (°C)
TLE	thermal linear expansion
ΔT_B	brittle temperature range
u	displacement (m)
v_c	casting speed
W	mold section size
b	body force vector
$[C]$	capacitance matrix
$[D]$, $\underset{\approx}{D}$	elasticity matrix/tensor
$\{F_{fp}\}$	force vector due to ferrostatic pressure
$\{F_q\}$	heat flow load vector
$[K]$	conductance matrix for heat-transfer model; stiffness matrix for stress model
$\hat{n}$	unit vector normal to the mold wall surface
$\{Q\}$	heat generation vector
$\underset{\approx}{\varepsilon}$, $\{\varepsilon\}$	strain tensor/vector
$\Delta\underset{\approx}{\hat{\varepsilon}}$	estimated of total strain increment
$\underset{\approx}{\sigma}$, $\{\sigma\}$	stress tensor/vector
$\underset{\approx}{\sigma}'$, $\{\sigma\}'$	deviatoric stress tensor/vector
$\underset{\approx}{\sigma}^*$, $\{\sigma\}^*$	stress tensor/vector without inelastic increament components
α	thermal expansion coefficient
ε	strain
$\overline{\varepsilon}$	equivalent strain
μ	lame constant
v	Poisson's ratio
ρ	density of steel (kg/m^3)
$\overline{\sigma}$	equivalent stress
σ_{yield}	yield stress (MPa)

Subscripts

flow	flow
in	inelastic
th	thermal
x	component along x direction
y	component along y direction
γ	austenite
δ	δ-ferrite
ε	elastic

REFERENCES

1. W.R. Storkman: Masters Thesis, University of Illinois, at Urbana-Champaign, Urbana, IL, 1990.
2. A. Moitra: Ph.D. Thesis, Urbana-Champaign, Urbana, IL, 1993, p. 217.
3. H. Zhu: Ph.D. Thesis, Urbana-Champaign, Urbana, IL, 1996, p. 132.

4. J.-C.T. Parkman: Master's Thesis, UIUC, Urbana, IL, 2000, p. 139.
5. W.R. Storkman and B.G. Thomas: in *Modeling of Casting and Welding Processes*, A.G. Giamei and G.J. Abbaschian, eds., Engineering Foundation, Palm Coast, FL, 1988, vol. 4, pp. 287-97.
6. A. Moitra, B.G. Thomas, and H. Zhu: in *76th Steelmaking Conf.*, Dallas, TX, 1993, ISS, Warrendale, PA, 1993, vol. 76, p. 657.
7. B.G. Thomas, A. Moitra, and W.R. Storkman: *Proc., 6th Int. Iron and Steel Congr.*, Iron and Steel Institute Japan, Tokyo, 1990, vol. 3, pp. 348-55.
8. B.G. Thomas and H. Zhu: *Proc. Int. Symp. on Advanced Materials and Technologies for 21st Century*, I. Ohnaka and D. Stefanescu, eds., TMS, Warrendale, PA, 1996, pp. 197-208.
9. G.D. Lawson, S.C. Sander, W.H. Emling, A. Moitra, and B.G. Thomas: *77th Steelmaking Conf.*, Chicago, IL, 1994, Iron and Steel Society, Warrendale, PA, 1994, p. 239.
10. B.G. Thomas, A. Moitra, and R. McDavid: *ISS Trans.*, 1996, vol. 23 (4), pp. 57-70.
11. B.G. Thomas and J.T. Parkman: *Thermec '97, Int. Conf. on Thermomechanical Processing of Steel and Other Materials*, Wollongong, Australia, 1997, TMS, Warrendale, PA, 1997, vol. II, pp. 2279-85.
12. B.G. Thomas and J.T. Parkman: *TMS Annual Meeting*, TMS, Warrendale, PA, San Antonio, TX, 1998, M.C.A.E. Lavernia, ed.
13. A. Grill, J.K. Brimacombe, and F. Weinberg: *Ironmaking and Steelmaking*, 1976, vol. 3 (1), pp. 38-47.
14. K. Sorimachi and J.K. Brimacombe: *Ironmaking and Steelmaking*, 1977, vol. 4 (4), pp. 240-45.
15. J.O. Kristiansson: *J. Thermal Stresses*, 1984, vol. 7, pp. 209-26.
16. J.E. Kelly, K.P. Michalek, T.G. O'Connor, B.G. Thomas, and J.A. Dantzig: *Metall. Trans. A*, 1988, vol. 19A, pp. 2589-2602.
17. J.R. Boehmer, G. Funk, M. Jordan, and F.N. Fett: *Adv. Eng. Software*, 1998, vol. 29 (7–9), pp. 679-97.
18. J.-k. Park, B.G. Thomas, and I.V. Samarasekera: *Ironmaking and Steelmaking*, 2002, vol. 29 (5), pp. 359-75.
19. M. Bellet, V.D. Fachinotti, O. Jaouen, S. De La Chapelle, I. Poitrault: in *Modeling of Casting, Welding and Advanced Solidification Processes-X,* D. Stefanescu, J. Warren, M. Jolly, and M. Krane, eds., TMS, Warrendale, PA, 2003, pp. 361-68.
20. J.-E. Lee, T.-J. Yeo, K.H. Oh, J.-K. Yoon, and U.-S. Yoon: *Metall. Mater. Trans. A*, 2000, vol. 31A, pp. 225-37.
21. K. Sorimachi and T. Emi: *Tetsu-to-Hagané (J. Iron Steel Inst. Jpn.)*, 1977, vol. 63 (8), pp. 1297-1304.
22. A. Grill and K. Schwerdtfeger: *Ironmaking and Steelmaking*, 1979, vol. 6 (3), pp. 131-35.
23. K. Kinoshita, T. Emi, and M. Kasai: *Tetsu-to-Hagané*, 1979, vol. 1979 (14), p. 2022.
24. F.G. Rammerstorfer, C. Jaquemar, D.F. Fischer, and H. Wiesinger: in *Numerical Methods in Thermal Problems*, R.W. Lewis and K. Morgan, eds., Pineridge Press, Swansea, U.K., 1979, pp. 712-22.
25. J.O. Kristiansson: *J. Thermal Stresses*, 1982, vol. 5 (3–4), pp. 315-30.
26. I. Ohnaka and Y. Yashima: in *Modeling and Control of Casting and Welding Processes IV*, Palm Coast, FL, 1988, TMS/AIME, Warrendale, PA, 1988, pp. 385-94.
27. T.C. Tszeng and S. Kobayashi: *Int. J. Machine Tools and Manufacture (Int. J. Machining Tools Manufacturing)*, 1989, vol. 29 (1), pp. 121-40.
28. H. Zhu: Ph.D. Thesis, University of Illinois, at Urbana-Champaign, Urbana, IL, 1997.
29. J. Parkman: Master's Thesis, University of Illinois, 2000.
30. C. Li and B.G. Thomas: *Brimacombe Memorial Symp.*, Vancouver, Canada, Canadian Institute of Mining and Metallurgy, Montreal, Canada, 2000, p. 17.
31. A.E. Huespe, A. Cardona, and V. Fachinotti: *Computer Methods Appl. Mech. Eng.*, 2000, vol. 182 (3), pp. 439-55.
32. A. Ramacciotti: *Steel Res.*, 1988, vol. 59 (10), pp. 438-48.
33. T.G. O'Conner: Ph.D. Thesis, University of Illinois, at Urbana-Champaign, Urbana, IL,1992.
34. J.-K. Park: Ph.D. Thesis, University of British Columbia, 2002.
35. B.G. Thomas: *74th Steelmaking Conf. Proc.*, ISS, Warrendale, PA, 1991, vol. 74, pp. 105-18.
36. B.G. Thomas: in *Making, Shaping and Treating of Steel: Continuous Casting*, A. Cramb, ed., AISE Steel Foundation, Pittsburgh, PA, 2003, vol. 5, pp. 5.1-5.24.
37. B.G. Thomas and L. Zhang: *Iron Steel Inst. Jpn. Int.*, 2001, vol. 41 (10), pp. 1185-97.
38. Y.M. Won and B.G. Thomas: *Metall. Mater. Trans. A*, 2001, vol. 32A, pp. 1755-67.
39. B.G. Thomas, G. Li, A. Moitra, and D. Habing: *Iron Steelmaker (ISS Trans.)*, 1998, vol. 25 (10), pp. 125-43.
40. B.G. Thomas: *Metall. Mater. Trans. B*, 2002, vol. 33B, pp. 795-812.
41. L. Yu: Master's Thesis, University of Illinois, at Urbana-Champaign, Urbana, IL, 2000.
42. Y. Won, T.-J. Yeo, D. Seol, and K. Oh: *Metall. Mater. Trans. B*, 2000, vol. 31B, pp. 779-94.
43. J.A. Dantzig and C.L. Tucker: *Modeling in Materials Processing*, Cambridge University Press, New York, NY, 2001.
44. O.C. Zienkiewicz and R.L. Taylor: *The Finite Element Method*, 5th ed., Butterworth-Heinemann, Oxford, Boston, MA, 2000, vol. 1, p. 689.
45. J. Lemaitre and J.L. Chaboche: *Mechanics of Solid Materials*, Cambridge University Press, New York, NY, 1990, p. 556.
46. R.C. Weast: *Handbook of Chemistry and Physics*, 1971.
47. E. Lemmon: in *Numerical Methods in Heat Transfer*, R.W. Lewis, K. Morgan, and O.C. Zienkiewicz, eds., John Wiley & Sons, New York, NY, 1981, vol. 1, pp. 201-13.
48. T. Dupont, G. Fairweather, and J.P. Johnson: *SIAM J. Numerical Analysis*, 1974, vol. 11 (2), pp. 392-410.
49. G.E. Forsythe and C.B. Moler: *Prentice-Hall Series in Automatic Computation*, Prentice-Hall, Englewood Cliffs, NJ, 1967.
50. A.M. Lush, G. Weber, and L. Anand: *Int. J. Plasticity*, 1989, vol. 5, pp. 521-49.
51. Y. Meng and B.G. Thomas: *Metall. Trans. B,* 2003, vol. 34B, pp. 685-705.
52. B.G. Thomas, G. Li, A. Moitra, and D. Habing: *80th Steelmaking Conf. Proc.*, ISS, Warrendale, PA, 1997, vol. 80, pp. 183-201.
53. B. Nour-Omid and P. Wriggers: *Computer Methods Appl. Mech. Eng.*, 1986, vol. 54, pp. 131-44.
54. J.M. Khodadadi, X.K. Lan, and F. Shen: ASME, New York, NY, American Society, *28th National Heat Transfer Conf. Exhib.*, San Diego, CA, 1992, vol. 196, pp. 59-67.
55. X. Huang, B.G. Thomas, and F.M. Najjar: *Metall. Trans. B*, 1992, vol. 23B, pp. 339-56.
56. Y.M. Won, K.-h. Kim, T.-j. Yeo, and K.H. Oh: *Iron Steel Inst. Jpn. Int.*, 1998, vol. 38 (10), pp. 1093-99.
57. M.C. Flemings: *Solidification Processing*, McGraw-Hill Series in Materials Science and Engineering, M.B. Bever, M.E. Shank, C.A. Wert, and R.F. Mehl, eds., McGraw-Hill, New York, NY, 1974, p. 364.
58. K. Harste: Ph.D. Thesis, Technical University of Clausthal, Clausthal, 1989, p. 115.
59. K. Harste, A. Jablonka, and K. Schwerdtfeger: *4th Int. Conf. Continuous Casting*, Brussels, Belgium, Verlag Stahleisen, Dusseldorf 1988, vol. 2, pp. 633-44.
60. I. Jimbo and A.A.W. Cramb: *Metall. Trans. B*, 1993, vol. 24B, pp. 5-10.
61. P. Kozlowski, B.G. Thomas; J. Azzi, and H. Wang: *Metall. Trans. A*, 1992, vol. 23A, pp. 903-18.
62. P.J. Wray: *Metall. Trans. A*, 1976, vol. 7A, pp. 1621-27.
63. P.J. Wray: *Metall. Trans. A*, 1982, vol. 13A, pp. 125-34.
64. T. Suzuki, K.H. Tacke, K. Wunnenberg, and K. Schwerdtfeger: *Ironmaking Steelmaking*, 1988, vol. 15 (2), pp. 90-100.
65. H. Mizukami, K. Murakami, and Y. Miyashita: *Tetsu-to-Hagané (J. Iron Steel Inst. Jpn.)*, 1977, vol. 63 (146), p. S-652.
66. C. Li and B.G. Thomas: in *Steelmaking Conf. Proc.*, ISS, Warrendale, PA, 2002, vol. 85, pp. 109-30.
67. J.H. Weiner and B.A. Boley: *J. Mech. Phys. Solids*, 1963, vol. 11, pp. 145-54.
68. T. Mathworks Inc.: *MATLAB User Manual*, Natick, MA, 1999, Ver. 5.3.
69. J.K. Park, C. Li, B.G. Thomas, and I.V. Samarasekera: *60th Electric Furnace Conf.*, San Antonio, TX, 2002, AIST, Warrendale, PA, 2002, vol. 60, p. 17.
70. C. Chow: Master's Thesis, University of British Columbia, 2001.
71. C. Li and B.G. Thomas: *Steelmaking Conf. Proc.*, ISS, Warrendale, PA, 2003, vol. 86.
72. C. Ojeda and B.G. Thomas: *ISSTech 2003*, Indianapolis, IN, 2003, ISS, Warrendale, PA, 2003.
73. R.D. Cook, D.S. Malkus, and M.E. Plesha: *Concepts and Applications of Finite Element Analysis*, 3rd ed., John Wiley & Sons, New York, NY, 1989, p. 630.
74. T.W. Clyne, M. Wolf, and W. Kurz: *Metall. Mater. Trans. B*, 1982, vol. 13B, pp. 259-66.
75. Y. Meng, C. Li, J. Parkman, and B.G. Thomas: in *Solidification Processes and Microstructures: A Symposium in Honor of Prof. W. Kurz,* M. Rappaz, C. Beckermann, and R. Trivedi, eds., TMS, Warrendale, PA, 2004, pp. 33-39.